

Probing Millicharged Particles at an Electron Beam Dump with Ultralow-Threshold Sensors

Rouven Essig,^a Peiran Li,^b Zhen Liu,^b Megan McDuffie,^{a,c} Ryan Plestid,^d Hailin Xu^{a,c}

^a*C.N. Yang Institute for Theoretical Physics, Stony Brook University, Stony Brook, NY 11794*

^b*School of Physics and Astronomy, University of Minnesota, Minneapolis, MN 55455, USA*

^c*Physics and Astronomy Department, Stony Brook University, NY 11794, USA*

^d*Walter Burke Institute for Theoretical Physics,
California Institute of Technology, Pasadena, CA 91125, USA*

E-mail: rouven.essig@stonybrook.edu, li001800@umn.edu, zliuphys@umn.edu,
megan.mcduffie@stonybrook.edu, rplestid@caltech.edu, hailin.xu@stonybrook.edu

ABSTRACT: We propose to search for millicharged particles produced in high-intensity electron beam dumps using small ultralow-threshold sensors. As a concrete example, we consider a Skipper-CCD placed behind the beam dump in Hall A at Jefferson Lab. We compute the millicharged particle flux, including both electromagnetic cascade and meson productions emanating from an aluminum target. We find that the sensitivity of a modest 2×14 array of Skipper-CCDs can exceed the sensitivity of all existing searches for millicharged particle masses below 1.5 GeV, and is either competitive or world leading when compared to other proposed experiments. Our results demonstrate that small-scale ultralow threshold silicon devices can enhance the reach of accelerator-based experiments, while fitting comfortably within existing experimental halls.

Contents

1	Introduction	1
2	Millicharged-particle production in electron beam dumps	2
2.1	Production of mCPs in the first radiation length	3
2.2	Production of mCPs in the electromagnetic cascade	4
2.3	Production of mCPs in meson decays	7
3	Detection with Low-Threshold Silicon Detectors	8
3.1	Conventional electron recoil detectors	8
3.2	Silicon detectors with \sim eV thresholds	9
3.3	Background estimates	10
4	Results	11
4.1	Pure millicharged particles	12
4.2	Dark matter interacting with an ultralight dark photon	14
5	Discussion and Conclusions	16
A	Dependence of electromagnetic shower simulation on energy threshold	16
A.1	Trident production	17
A.2	Annihilation production	17
B	Multiple scattering	18
C	Beam-induced neutron backgrounds	18

1 Introduction

Extensions of the Standard Model (SM) are well motivated due, for example, to the observed dark matter relic abundance of our universe, the presence of neutrino masses, and the observed baryon asymmetry of the universe. New physics may be strongly coupled, in which case it must be heavy and is best searched for at high-energy colliders. However, extremely feebly coupled dark sectors are viable even for masses smaller than ~ 1 GeV. In this regime, beyond the SM (BSM) physics can be efficiently searched for in high-intensity accelerator experiments [1–8].

A simple extension of the Standard Model is a particle with a small electric charge (e.g., a particle with small hypercharge that is a singlet under $SU(2)$). Such particles are often referred to as millicharged particles (mCPs); they have interesting cosmological signatures and, if they compose the dark matter, novel direct-detection prospects [9–21]. The existence of mCPs has interesting consequences related to charge quantization and grand unified theories [22, 23], and “effective mCPs” naturally arise via kinetic mixing in the presence of a light, but massive, dark photon [24, 25].

Searches for mCPs using accelerator facilities [2–8, 26–32] or cosmic-ray production [33–38] are completely agnostic to astrophysical assumptions that can hamper searches for mCP dark matter. They can, therefore, easily probe models with an mCP in their spectrum without any astrophysical, cosmological, or model-dependent uncertainties. Currently, the strongest constraints below ~ 2 GeV in mass come from a combination of accelerator-based experiments [8, 39]. The strongest published constraints on mCPs with

masses below ~ 100 MeV are obtained from the SLAC-mQ collaboration [2], a reanalysis of LSND’s $\nu e \rightarrow \nu e$ scattering dataset [3, 4], and a recent search by the SENSEI collaboration using data taken in the MINOS hall at Fermilab [8].

The SLAC-mQ experiment used a 29.5 GeV electron beam on a 6 radiation-length target consisting of 75% tantalum and 25% rhenium, with a detector placed downstream at a distance of 82.6 m [2]. The success of the SLAC-mQ experiment strongly motivates a renewed study of high-intensity electron beam dumps. In particular, we are motivated by the proposed Beam Dump Experiment (BDX) in the Continuous Electron Beam Accelerator Facility (CEBAF) at Jefferson Lab [40–43]. The BDX collaboration plans to deliver 10^{22} electrons on target (EOT) over six months, which is three orders of magnitude larger than the 8.4×10^{18} EOT delivered in the SLAC-mQ experiment.

Besides increasing the EOT, we advocate here for using ultralow-threshold sensors. This is motivated by the fact that mCPs that scatter in a detector medium prefer to transfer very little energy to it. Moreover, the SENSEI collaboration performed an opportunistic search for mCPs using their Skipper-CCD detector, which happened to be located downstream of the NuMI beam in the MINOS cavern at Fermilab [8]. Despite the fact that only a single 2-gram Skipper-CCD was in operation and the SENSEI detector was ~ 1 km away from the target, the low-energy threshold of the Skipper-CCD enhances the sensitivity to mCPs compared to a typical detector that has a much higher threshold, and world-leading limits were placed on mCPs. The Oscura collaboration has proposed using a 1-kg Skipper-CCD detector to search for mCPs using the NuMI beam as part of an engineering test on the way to developing a 10-kg dark matter detector [44]. Skipper-CCDs have also been used in mCP searches produced in reactors [45].

In this paper, we study the sensitivity of small, low-threshold sensors placed downstream from an electron beam-dump facility. Following the success of the SENSEI search [8], Skipper-CCDs are an obvious example, but other low-threshold sensors used in sub-GeV dark matter searches are also good candidates. This includes the SuperCDMS HVeV detectors, which consist of transition edge sensor (TES) attached to a silicon crystal [21, 46, 47], or the detectors used by the EDELWEISS collaboration, such as a neutron-transmutation-doped (NTD) thermal sensor glued to a germanium crystal [20]. For concreteness, we focus in this paper on a silicon detector.

A significant advantage of low-threshold detectors is that they are small and versatile, and relatively easy to deploy. We study different production modes, first matching and then exceeding the sophistication of the SLAC-mQ target simulation (i.e., we include new production modes). Next, we argue that a zero-background search with a small Skipper-CCD detector is possible and that the sensitivity of a BDX-like setup would have world-leading sensitivity to mCPs across a wide range of masses.

The rest of the paper is organized as follows. In Section 2, we outline the dominant mCP production modes both in the first radiation length and in the ensuing electromagnetic cascade, including also production from meson decays. Next, in Section 3, we discuss the detector scattering cross section for both high- and low-energy threshold detectors, emphasizing the role of the plasmon resonance for the latter. This leads naturally to Section 4, where we present our results for the reach of a Skipper-CCD detector downstream of a BDX-like electron beam dump. In Section 5, we summarize our findings and outline potentially interesting future directions. Three appendices provide additional details. In Appendix A, we discuss additional details for the mCP production. In Appendix B, we estimate the scattering angle of mCP interacting in the shield before reaching the detector volume. In Appendix C, we provide estimates of beam-and cosmic-ray induced backgrounds.

2 Millicharged-particle production in electron beam dumps

In this section, we calculate the flux of mCPs emanating from an electron beam-dump target before discussing the detection of mCPs in Section 3. For concreteness, we use benchmarks that are motivated by BDX: 10^{22} EOT, a 10.6 GeV electron-beam energy, and a 300 cm thick aluminum target [40, 41].

We organize the calculation as follows: First, we discuss trident production of mCPs, χ and $\bar{\chi}$, in an electron (e^-) beam interacting with aluminum nuclei A ($e^- A \rightarrow e^- A \chi \bar{\chi}$) in the first radiation length of the

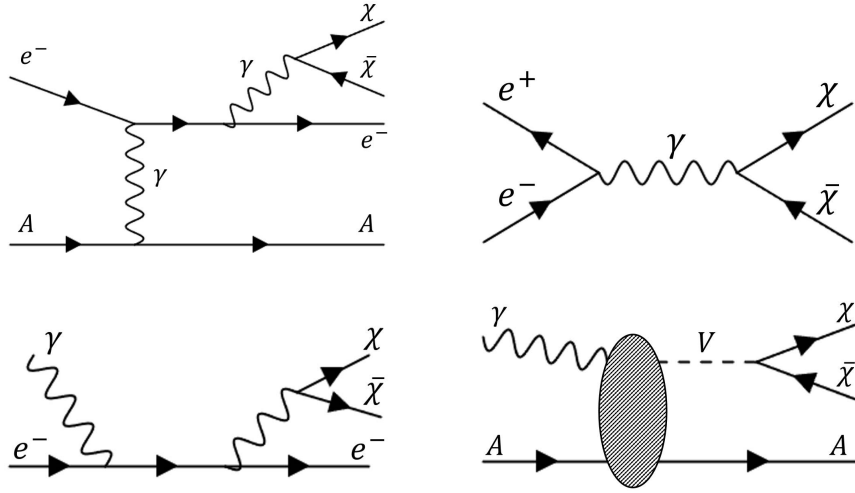


Figure 1. The leading Feynman diagrams for the production of mCPs (χ) in an electron beam incident on a target containing nuclei A . **Top left:** trident production ($e^- A \rightarrow e^- A \chi \bar{\chi}$); **Top right:** electron-positron annihilation ($e^+ e^- \rightarrow \chi \bar{\chi}$); **Bottom left:** Compton production ($\gamma e^- \rightarrow e^- \chi \bar{\chi}$); **Bottom right:** vector meson production with decay ($\gamma A \rightarrow A \chi \bar{\chi}$), which we treat in the narrow-width approximation. Both electron-positron annihilation production and Compton production involve secondary positrons and photons from the electromagnetic shower.

target. Next, we consider the electromagnetic cascade and production stemming from daughter photons, electrons, and positrons. This matches the sophistication of the SLAC-mQ experiment for the trident production channel, and further includes two new production mechanisms: positron annihilation ($e^+ e^- \rightarrow \chi \bar{\chi}$) and Compton production ($\gamma e^- \rightarrow e^- \chi \bar{\chi}$). We find that the production of mCP via annihilation can dominate over the trident mechanism in certain regions of parameter space (for $2 \text{ MeV} \lesssim m_\chi \lesssim 50 \text{ MeV}$); however, we also find that the Compton production is always subdominant. Finally, we estimate the photonuclear production channels, which dominates the flux at larger mCP masses (specifically for $m_\chi \gtrsim 130 \text{ MeV}$). We show the leading Feynman diagrams for the dominant four production modes in Fig. 1.

2.1 Production of mCPs in the first radiation length

In the first radiation length, the leading channel of mCP production from the 10.6 GeV electron beam is the trident process

$$e^- A \rightarrow e^- A \chi \bar{\chi},$$

where A is the aluminum nucleus. One of the leading Feynman diagram topologies is shown in Fig. 1 (top-left). The computation of this $2 \rightarrow 4$ process is performed using `MadGraph5_aMC@NLO` [48]. The electromagnetic coupling between the Al nucleus and mCP is implemented via `FeynRules` [49] with an atomic form factor (the terms involving a and a'), a nuclear form factor (the term involving d) for coherent scattering, and a nucleon form factor (the term involving μ_p) for incoherent scattering [1, 50–52], as follows

$$|F(t)|^2 = Z^2 \left(\frac{a^2 t}{1 + a^2 t} \right)^2 \left(\frac{1}{1 + t/d} \right)^2 + Z \left(\frac{a'^2 t}{1 + a'^2 t} \right)^2 \left(\frac{1 + \frac{t}{4m_p^2} (\mu_p^2 - 1)}{\left(1 + \frac{t}{0.71 \text{ GeV}^2}\right)^4} \right)^2.$$

Here, Z is the atomic number, $a = 111 Z^{-1/3}/m_e$, $a' = 773 Z^{-2/3}/m_e$, $d = 0.164 \text{ GeV}^2 A^{-2/3}$ with atomic mass number A , $\mu_p = 2.79$, $m_p = 0.938 \text{ GeV}$ is the proton mass, and $t = -q^2$ with q^2 the four-momentum transfer squared (note that $t \geq 0$).

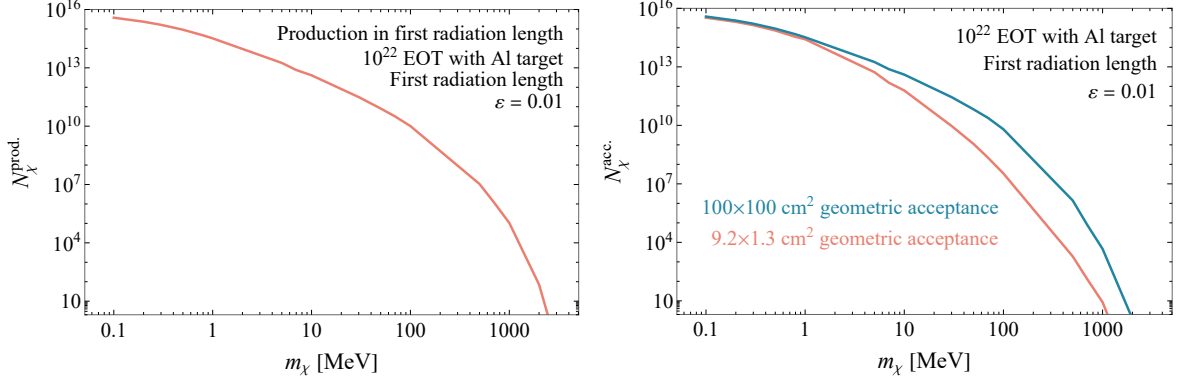


Figure 2. Left: The number of mCPs produced from trident production $e^- N \rightarrow e^- N \chi \bar{\chi}$ in the first radiation length versus the mCP mass m_χ from a 10.6 GeV electron beam incident on a thick aluminum target. The millicharge is chosen to be $\varepsilon = 0.01$ (in units of the electron charge). **Right:** The number of mCPs produced from trident production in the first radiation length and passing through a $9.2 \times 1.3 \text{ cm}^2$ or $100 \times 100 \text{ cm}^2$ area along the beam center 20 m downstream of the target, where our representative silicon detector will be located.

As a useful benchmark against other lepton beam-dump studies in the literature [53, 54], we consider the mCP flux produced in the first radiation length. This approach offers a conservative lower-bound on the mCP flux and is a useful approximation at the order-of-magnitude level. As we will see below, including the full electromagnetic cascade and other production channels further increases the flux of mCPs.

The total number of mCPs produced in the first radiation length is computed using

$$N_\chi^{\text{prod.}} = 2 \cdot N_{\text{EOT}} \cdot \frac{\rho \cdot N_A}{M_{\text{atom}}} \cdot X_0 \cdot \sigma_{\text{prod.}}, \quad (2.1)$$

where $N_{\text{EOT}} = 10^{22}$ is the number of electrons on target [43], $X_0 = 8.89 \text{ cm}$ is the radiation length of aluminum [55], $\rho = 2.7 \text{ g/cm}^3$ is the density of the aluminum target, $M_{\text{atom}} = 27 \text{ g/mol}$ is the molar mass of aluminum, N_A is the Avogadro constant, and $\sigma_{\text{prod.}}$ is the cross section of the trident production with a 10.6 GeV electron beam.

In the first-radiation-length approximation, the total number of mCPs and the number of mCPs within the detector geometric acceptance are shown in the left and right plot of Fig. 2, respectively. The geometric acceptance assumes a detector placed 20 m downstream on the beam line with rectangular areas of $9.2 \text{ cm} \times 1.3 \text{ cm}$ and $1 \text{ m} \times 1 \text{ m}$; these correspond, respectively, to the size of a single Skipper-CCD used in the SENSEI search [8], and the transverse dimensions of the nominal BDX detector [43]. As m_χ increases, the signal cross section decreases. Furthermore, heavier mCPs are less forward through trident production and, hence, have a reduced geometric acceptance.

2.2 Production of mCPs in the electromagnetic cascade

The electromagnetic (EM) cascade includes all of the secondary Quantum Electrodynamics (QED) particles that are generated when the incident 10.6 GeV electron passes through the target. This includes photons, which are emitted as bremsstrahlung, and all of their subsequent descendants, which are electrons, positrons, and photons. The mCPs generated by these three particles can be classified into three production modes—trident production, annihilation of positrons with atomic electrons, and Compton scattering. We discuss each of them below, but note that Compton scattering is subdominant; the leading Feynman diagram for each process is shown in Fig. 1. We simulate the SM EM cascade using PETITE [56], combined with a set of MadGraph simulations for the mCP production channels.

Trident production in a nuclear field

A single 10.6 GeV electron on target generates from the EM shower about 200 photons, 450 electrons, and 300 positrons, each with energy above 10 MeV.¹ Just like the primary electron beam, the secondary electrons and positrons can produce mCPs from trident processes. For each electron/positron in the shower, the number of mCPs from trident production is

$$N = 2 \cdot \frac{\rho \cdot N_A}{M_{\text{atom}}} \cdot \lambda_{\text{MFP}} \cdot \sigma(E_e), \quad (2.2)$$

where $\lambda_{\text{MFP}}(E_e)$ is the mean-free path of the electron/positron, and $\sigma(E_e)$ is the production cross section, both for an incident electron/positron with energy E_e . The cross section $\sigma(E_e)$ is computed via **Madgraph**. For large mCP masses, as the energy decreases, the cross section decreases due to phase space suppression. For small mCP masses, the cross section also drops as the energy decreases, which can be understood within the context of the Weizsäcker-Williams approximation [1, 57, 58].

In general, as the energy of the secondary particles decreases, the mCPs are produced with larger angles relative to the beam line. Therefore, mCPs that originate from low-energy secondary particles will have a small geometric acceptance at the detector. In our analysis, we ignore all secondary particles that have an energy below 10 MeV. We checked that the mCPs produced from secondary particles with energies below 10 MeV are negligible, and we provide the relevant details in [Appendix A](#). The number of mCPs produced in trident processes for different mCP masses m_χ are shown with the red curves in [Fig. 3](#), both without (left plot) and with (right plot) the detector acceptance.

Given that we can ignore secondary particles with energy below 10 MeV, we note that the precise thickness of the aluminum target (which is 300 cm) is not important, as long as it is thicker than about 10 radiation lengths (~ 90 cm), as after 10 radiation lengths, the secondary particles will have an average energy of $\sim 10 \text{ GeV} \times (1/2)^{10} \lesssim 10 \text{ MeV}$.

Annihilation of positrons with atomic electrons

Inside a material, high-energy photons pair-produce electrons and positrons in the Coulomb field of nuclei. When positrons propagate through the material, they can annihilate to mCPs, $e^+e^- \rightarrow \chi\bar{\chi}$. This is an important production mechanism, since the cross section per atom is proportional to $Z \times (\alpha^2 \varepsilon^2)$ as compared to $\alpha^4 Z^2$ for trident production, where $\alpha \simeq 1/137$ is the fine-structure constant. The annihilation cross section is

$$\sigma_{\text{anni.}} = \frac{4\pi\alpha^2\varepsilon^2}{3} \frac{(s + 2m_e^2)}{s^3\sqrt{s - 4m_e^2}} (s + 2m_\chi^2) \sqrt{s - 4m_\chi^2},$$

where $s = 2m_e E + m_e^2$ is the center-of-mass-energy squared. The production rate is proportional to s^{-1} for light mCPs. For heavy mCPs, the cross section will rapidly decrease near the kinematic threshold. We show the mCP production from annihilation in the yellow line in [Fig. 3](#), both without (left) and with (right) the detector acceptance, which exhibits these features clearly. Furthermore, looking at the right panel of [Fig. 3](#), the annihilation process is a dominant channel for m_χ between 2 MeV to 50 MeV. This is because the annihilation process produces mCPs at smaller angles compared to the trident process, which are more spread out. For a given incident positron with momentum p_z , the boost of the mCPs from electron-positron annihilation is the three-momentum of the photon propagator, which also equals p_z . As m_χ increases, the number of mCPs traversing the detector even increases slightly, since the transverse momentum of the mCP decreases.

Compton production off atomic electrons

Photons produced in the EM cascade can Compton scatter off atomic electrons and produce mCPs. We find that Compton production of mCPs is subdominant to the mCPs produced in both trident processes

¹Note that this counting is sensitive to the infrared cut off, and we count every particle once per (forward-dominant) scattering in the Monte Carlo.

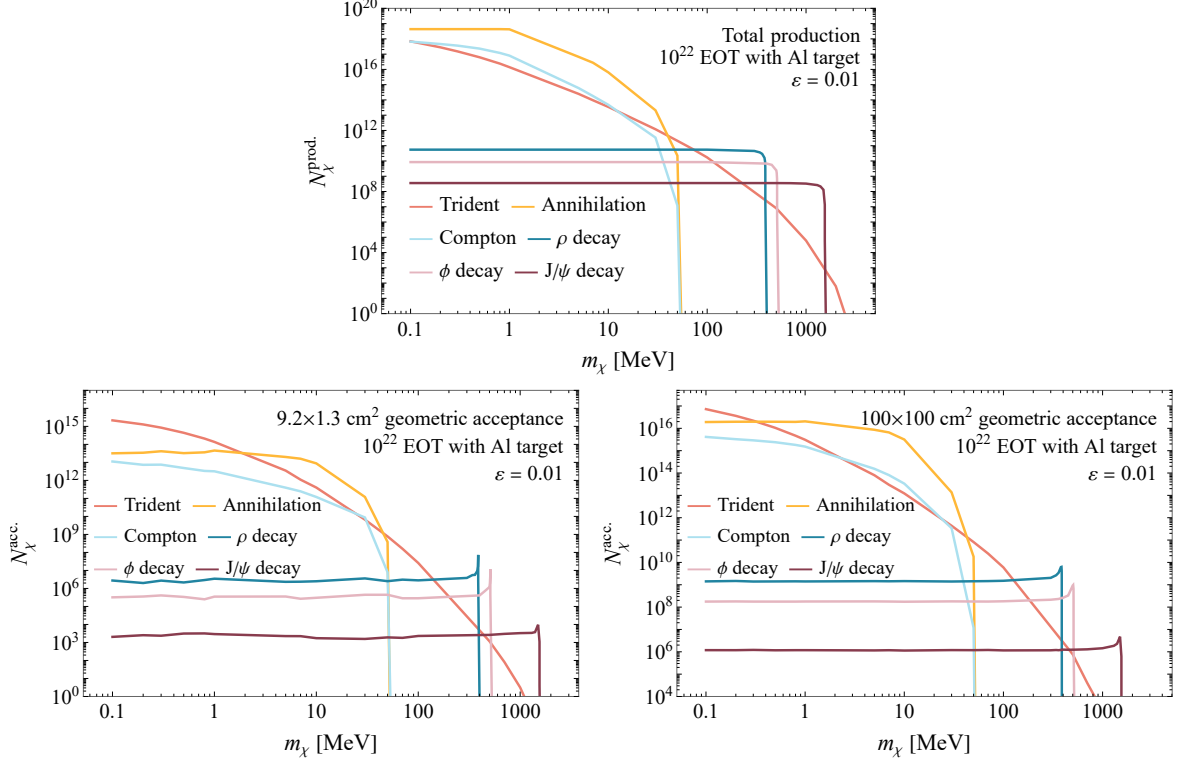


Figure 3. Top: The number of mCPs produced versus the mCP mass m_χ from a 10.6 GeV electron beam incident on a thick aluminum target. The millicharge is chosen to be $\varepsilon = 0.01$ (in units of the electron charge). The mCPs are produced in trident processes (red), electron-positron annihilation (yellow), Compton scattering (light blue), and various meson decays (ρ (blue), ϕ (pink), and J/Ψ (dark red)). The inclusion of the EM cascade increases the trident yield by a few (roughly $\sim 2\times$ more mCPs) compared to the mCPs produced in the first radiation length (see Fig. 2), whereas e^+e^- annihilation and meson decays introduce qualitatively new features that dominate the flux for different m_χ . **Bottom left:** The total number of mCPs that pass through an area of $9.2 \times 1.3 \text{ cm}^2$ at a distance 20 m downstream of the target on the beam line, where our representative silicon detector will be located. The sharp “peaks” near the meson thresholds arise from the increased acceptance due to the small p_T imparted in the meson decay to the mCP pairs. **Bottom right:** The total number of mCPs that pass through an area of $100 \times 100 \text{ cm}^2$ at a distance of 20 m downstream of the target on the beam line.

and electron-positron annihilation. The production cross section is computed numerically via **MadGraph** in this study. To understand the result, here we provide a parametric estimation via the annihilation process convolved with a splitting function,

$$\sigma_{\text{Comp.}} = \frac{\alpha}{2\pi} \ln\left(\frac{s}{m_e^2}\right) \int_{x_{\min}}^1 dx P_{\gamma \rightarrow ee}(x) \sigma_{\text{anni.}}(xs),$$

where $P_{\gamma \rightarrow ee}(x) = x^2 + (1-x)^2$ is the splitting function for the incident photon to produce an electron-positron pair, and $x_{\min} \approx 4m_\chi^2/s$. Both annihilation and Compton production have the same energy threshold, which is set by m_χ , as shown explicitly in Fig. 3. The leading-logarithm $\ln\left(\frac{s}{m_e^2}\right)$ provides a factor of $\mathcal{O}(10)$ enhancement, but $\frac{\alpha}{2\pi}$ gives a suppression of $\sim 10^{-3}$. Thus, the Compton production is generally smaller than annihilation by about two orders of magnitude.

2.3 Production of mCPs in meson decays

As a final production mode, we include an estimate of photonuclear reactions that source mesons, which subsequently decay into $\chi\bar{\chi}$ pairs; we specifically focus on the production of vector mesons. We have verified that the yield of pseudoscalar mesons produced via Primakoff scattering is subdominant to the electromagnetic cascade across the full range of available mCP masses. In contrast, vector-meson production is significantly larger than pseudoscalar meson production, which is in agreement with estimates produced for LDMX and NA64 [59]. Moreover, vector mesons can produce more mCPs than those produced in the EM cascade, at least for $m_\chi \gtrsim 130$ MeV. We, therefore, study $\gamma \rightarrow \rho, \phi, J/\psi$ production modes.

We focus first on the photoproduction of ρ mesons. Since the ρ mass is relatively heavy, production occurs dominantly in the first radiation length of the target. The ρ is produced from an approximately equal mixture of coherent and incoherent processes. For simplicity, in the discussion that follows, we focus on the coherent channel; however, we include both coherent and incoherent production (i.e., on individual nucleons) in our estimates. We only include photons from the first radiation length, which will underestimate the full flux by a factor of a few.

In the complete screening approximation (appropriate for $E_e \simeq 10$ GeV), the number of photons produced per radiation length per energy interval dE_γ is given by [60]

$$\frac{dN_\gamma}{dE_\gamma} \simeq \frac{N_{\text{EOT}}}{E_\gamma} \left[\frac{4}{3} \left(1 - \frac{E_\gamma}{E_e} \right)^2 + \left(\frac{E_\gamma}{E_e} \right)^2 \right]. \quad (2.3)$$

We multiply this expression by the probability for a photon to produce a ρ meson instead of converting into a e^+e^- pair. When considering coherent production, $E_\rho \simeq E_\gamma$, and so we have

$$\frac{dN_\rho}{dE_\gamma} = \frac{dN_\gamma}{dE_\gamma} \times \frac{\sigma_{\text{coh.}}(E_\gamma)}{\sigma_{\text{pair}}(E_\gamma)}. \quad (2.4)$$

A similar formula holds for incoherent scattering, but the energies of the meson can be less than that of the incident photon, since the momentum transfer can be larger than in the coherent reaction. Following [59], we take $\sigma_{\text{coh.}}(E_\gamma) = Af_{\text{coh.}} \times \sigma_{\gamma p \rightarrow \rho p}(E_\gamma)$, where $\sigma_{\gamma p \rightarrow \rho p}$ is the photoproduction cross section on a free proton, and A is the number of nucleons inside the nucleus. A similar formula defines the incoherent cross section, $\sigma_{\text{inc.}}(E_\gamma) = Af_{\text{inc.}} \times \sigma_{\gamma p \rightarrow \rho p}(E_\gamma)$. A detailed estimate including final-state interactions using a Glauber optical model for $A = 27$ is given in [59] from which we take $f_{\text{coh.}} = 0.57$ and $f_{\text{inc.}} = 0.35$ for ρ -meson production in all of our numerical estimates. We use a similar procedure as above to estimate ϕ meson photoproduction, with $f_{\text{coh.}} = 0.33$ and $f_{\text{inc.}} = 0.65$ again following [59]. We use the smooth fit of ρ and ϕ photoproduction from Fig. 1 of [61] and demand $E_\gamma \geq 2$ GeV.

The coherent reaction limits the momentum transfer to small values with a characteristic scale set by the inverse nuclear radius $1/R_{\text{A}1} \simeq 55$ MeV. This leads to small deflection angles that can be neglected when compared to the emission angle of χ or $\bar{\chi}$, which is set by the boost of the decaying meson, $\theta_\chi \sim m_\rho/E_\rho$. Incoherent scattering has larger momentum transfers ($|Q| \lesssim \text{GeV}$); however, the mesons can still be treated as approximately forward-going (i.e., at small angles relative to the beam axis), since the decay angle dominates the final angle of the χ or $\bar{\chi}$ particle which later scatters in the detector. We, therefore, treat all photoproduced ρ and ϕ mesons as forward-going (i.e., we neglect their angle with respect to the beam axis when generating $\chi\bar{\chi}$ samples). Transverse momentum from the photoproduction of the parent meson is only important when the meson mass is close to $2m_\chi$, and we include this effect in our simulations.

Given a sample of ρ and ϕ mesons, we simulate their two-body decays into $\chi\bar{\chi}$ in the rest frame and boost the mCPs to the lab frame in order to get the total flux within the detector geometric acceptance (shown in Fig. 3). The contributions from meson decays peak near their kinematic thresholds after accounting for geometric acceptance effects, because the three-momentum of mCPs becomes small in the meson rest frame, making it easier to boost these mCPs into the forward region. In this near-threshold region, the transverse momentum distribution of the parent meson determines the height of the ‘‘peaks’’ that can be seen in Fig. 3.

For $m_\chi \geq m_\phi/2 \simeq 510$ MeV, the decay of ϕ mesons is kinematically forbidden. The next relevant meson is the J/ψ . The larger meson mass, $m_{J/\psi} \approx 3.1$ GeV, suppresses the coherent contribution to the cross section

such that incoherent scattering (i.e., on individual nucleons) dominates the rate. Again following [59] we simply take a naive model of incoherent scattering on A independent nucleons at rest, since final-state interactions and other nuclear effects are expected to be small [59]. The momentum transfers in the incoherent scattering are such that the energy of the J/ψ differs substantially (i.e., by a few GeV) from the energy of the incident photon.

To generate a sample of J/ψ mesons we rely on recent data on J/ψ production on a proton [62] and demand $E_\gamma \geq 8.5$ GeV. First, we draw photons from the weighted distribution

$$\frac{dN_{\gamma \rightarrow J/\psi}}{dE_\gamma} = \frac{dN_\gamma}{dE_\gamma} \frac{A \times \sigma_{J/\psi}(E_\gamma)}{\sigma_{\text{pair}}(E_\gamma)}, \quad (2.5)$$

where $\sigma_{J/\psi}(E_\gamma)$ is the photoproduction cross section on a free proton [62]. Given a fixed photon energy, we then sample $Q^2 = |t|$ from the distribution $1/(1+Q^2/m_s^2)^4 \Theta(Q^2 - Q_{\text{min}}^2) \Theta(Q_{\text{max}}^2 - Q^2)$, where $m_s \approx 1.4$ GeV is fit from data [62] (we take m_s to be independent of energy for simplicity). The Heaviside functions enforce the minimal and maximal Q^2 given the kinematics. We find that the first generation of photons from 10^{22} EOT will produce roughly 6×10^{13} J/ψ mesons in one radiation length. In the limit where $m_\chi \ll 1.5$ GeV, this then leads to roughly $\varepsilon^2 \times (5 \times 10^{12})$ mCPs produced via $J/\psi \rightarrow \chi \bar{\chi}$.

The conversion from the J/ψ Monte Carlo sample to a flux of χ and $\bar{\chi}$ passing through the detector is handled in the same manner as for ρ and ϕ mesons. As shown in Fig. 3, the J/ψ decay channel dominates the production rate when $m_\chi \gtrsim 500$ MeV. This channel effectively determines the mass-reach of the electron beam dump setup we consider and there is a rapid loss in sensitivity for $m_\chi \gtrsim 1.55$ GeV.

Our treatment of meson photoproduction is a conservative underestimate of the flux (in contrast to our treatment of the EM cascade production modes, which is realistic). We have only included photoproduction in the first radiation length, and we have neglected direct electroproduction (e.g., $e p \rightarrow e J/\psi p$). A more detailed simulation of photonuclear-induced meson decays at electron beam dump facilities will be pursued in future work, both for mCPs and, more generally, for dark sectors.

Finally, before moving onto mCP detection, let us comment on the propagation of mCPs through matter. Multiple Coulomb scattering of charged particles can lead to angular spreading which would influence the geometric acceptance plotted in Fig. 3. Between the aluminum target and the detector hall/well, there is 5.4 m of concrete and 14.2 m of dirt [63]. In Appendix B we provide a short discussion of multiple Coulomb scattering, and conclude that it does not significantly affect the angular distribution, and by proxy our sensitivity projections, for $\epsilon \lesssim 0.01$. We therefore do not include multiple Coulomb scattering in the intervening dirt and concrete between the target and the detector in any of the results that follow.

3 Detection with Low-Threshold Silicon Detectors

Having discussed the production of mCP pairs in an electron beam-dump target, we now discuss how to detect them. We first discuss detecting mCPs using conventional (high-threshold) detectors, which have the advantage of being large, but the disadvantage of having higher thresholds, larger footprints, and being more expensive. We then outline how low-threshold sensors can offer improved detection prospects for mCPs, focusing on silicon sensors. We comment on backgrounds, such as beam-induced or cosmic-ray induced spallation neutrons, as well as cosmic-ray backgrounds more generally.

3.1 Conventional electron recoil detectors

When electron recoil energies, ω , are large compared to atomic scales ($\omega \gg 1$ keV), we can approximate the electron as being free. The differential cross section for an mCP to scatter off a free electron is given by [27, 64],

$$\left. \frac{d\sigma}{d\omega} \right|_{E_\chi \gg \omega, m_\chi, m_e} = \pi \alpha^2 \varepsilon^2 \frac{2E_\chi^2 m_e + \omega^2 m_e - \omega(m_\chi^2 + m_e(2E_\chi + m_e))}{\omega^2(E_\chi^2 - m_\chi^2)m_e^2} \Big|_{E_\chi \gg \omega, m_\chi, m_e} \simeq \frac{2\pi \alpha^2 \varepsilon^2}{\omega^2 m_e}. \quad (3.1)$$

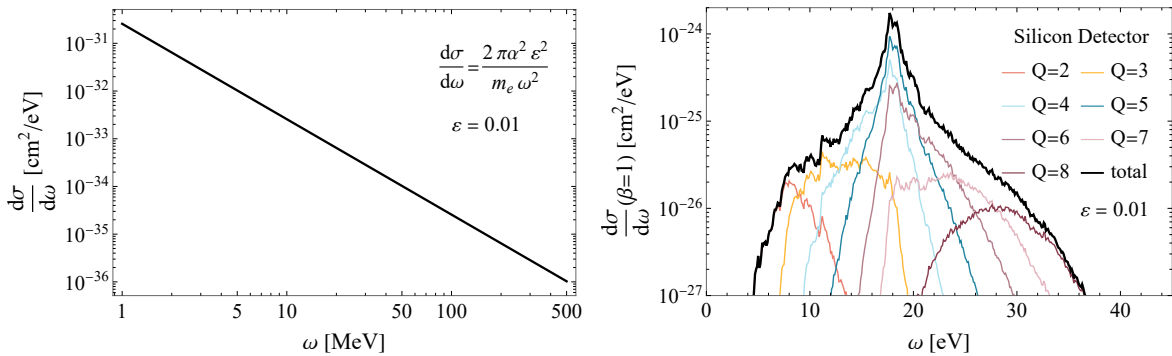


Figure 4. **Left:** Differential cross section per target electron for a relativistic mCP to scatter off a free electron ($\beta = 1$). We set the millicharge to $\varepsilon = 0.01$. **Right:** Differential cross section per target electron for a relativistic mCP interacting with silicon ($\beta = 1$). The black line shows the total cross section, while the colored lines show the cross section of producing an event with a specific charge Q , ranging from $Q = 2e^-$ to $Q = 8e^-$.

This differential cross section can be integrated to give the total cross section (denoted here as σ_0) for a recoil energy between ω^{\min} and ω^{\max} [27],

$$\sigma_0 = \pi\alpha^2\varepsilon^2 \frac{m_e(\omega^{\max} - \omega^{\min})(2E_\chi^2 + \omega^{\max}\omega^{\min}) - \omega^{\max}\omega^{\min}(m_\chi^2 + m_e(2E_\chi + m_e)) \log \frac{\omega^{\max}}{\omega^{\min}}}{\omega^{\max}\omega^{\min}(E_\chi^2 - m_\chi^2)m_e^2}. \quad (3.2)$$

Given the number of electrons in a detector, and the detection cross section, σ_0 , one can compute the number of events per 10^{22} EOT. An important feature of Eq. (3.2) is that the cross section scales as $1/\omega^{\min}$, which leads to the well-known observation that low-threshold detectors have an increased sensitivity to mCPs. Fig. 4 (left) shows the differential scattering cross section versus the electron recoil energy ω assuming the free-electron approximation. In Section 3.2, we will see that this is orders of magnitude below the peak of the scattering cross section (located near $\omega \sim 18$ eV) in a silicon detector (see Fig. 4, right).

The proposed BDX detector includes an electromagnetic calorimeter consisting of PbWO_4 . The planned location is 20 m downstream (and centered on the beamline) of the aluminum target with geometric dimensions given by $\sim 1 \text{ m} \times 1 \text{ m} \times 1 \text{ m}$. For the BDX-mini experiment, which used PbWO_4 crystals totaling a volume of $\sim 4 \times 10^{-3} \text{ m}^3$, it was found that an energy threshold of ~ 300 MeV is required to achieve zero cosmic-ray backgrounds [43, 65]. Even if the 300 MeV energy threshold is sufficient to achieve zero backgrounds for the larger 1 m^3 detector, and despite its much larger geometric acceptance and detector mass, the mCP scattering cross section is very suppressed when compared to the peak cross section in a silicon detector, which lies below 50 eV. We will illustrate the reach of such a setup (1 m^3 detector, 300 MeV threshold) in Section 4, finding that it is much weaker than a small ($\mathcal{O}(10 \text{ cm}^2)$), gram-scale silicon detector with a few-eV threshold.

Given the large increase in the scattering cross section for lower energy thresholds, it is interesting to ask at what threshold a hypothetical background-free 1 m^3 detector is comparable to a small, gram-scale low-threshold silicon detector. We will see in Section 4, that an energy threshold of about 10 MeV will allow for a comparable sensitivity provided that a zero-background search can be carried out with the same 10 MeV energy threshold.

3.2 Silicon detectors with $\sim \text{eV}$ thresholds

Low-threshold sensors used for sub-GeV dark matter detection are also suitable for probing mCPs produced in colliding-beam, fixed-target, or beam-dump experiments. Although one might naively expect that the high energy of the mCP will also produce a high-energy signal in a detector, we saw in Section 3.1 that the mCP scattering rate is highly suppressed at large recoil energies. Instead, the signal peaks towards low energies. As

we will review below, when a relativistic mCP scatters in a silicon detector target, it will typically produce events containing a few electron-hole pairs (which we will simply denote as “ e^- ”); in fact, the majority of the signal events will contain a charge Q of $4e^- - 6e^-$. Low-threshold sensors, such as Skipper-CCDs [8, 66] and other silicon or germanium detectors with TES or NTD readout [20, 21, 46, 47] have demonstrated single electron-hole pair resolution, and are capable of observing such signals.

To calculate the cross section of relativistic mCPs in a sensor, we focus on silicon and use the formalism in [67], which uses the dielectric function of a material. For a mCP particle with velocity β , the differential cross section (per electron) to deposit energy between ω and $\omega + d\omega$ in the target is given by

$$\frac{d\sigma}{d\omega}(\omega, \epsilon) = \frac{2\alpha\epsilon^2}{n_e\pi\beta^2} \int_{k_{\min}}^{k_{\max}} dk \left\{ \frac{1}{k} \text{Im} \left(\frac{-1}{\epsilon(\omega, k)} \right) + k \left(\beta^2 - \frac{\omega^2}{k^2} \right) \text{Im} \left(\frac{1}{-k^2 + \epsilon(\omega, k)\omega^2} \right) \right\}, \quad (3.3)$$

where α is the fine structure constant, n_e is the number density of free electrons in the target ($\sim 0.685 \text{ \AA}^{-3}$ for silicon), k is the momentum transfer of the mCP to the target, and $\epsilon(\omega, k)$ is the dielectric function. The integration of the momentum transfer k is kinematically constrained to be between $k_{\min} = \omega/\beta$ and $k_{\max} = 2|\mathbf{p}| - k_{\min}$, where \mathbf{p} is the momentum of the incoming mCP particle. The term $\text{Im}(-1/\epsilon(\omega, k))$ is the electron loss function (ELF), which describes the interaction of the mCP with the target through the exchange of a longitudinal-mode photon, which dominates in the context of non-relativistic scattering. In relativistic scattering, we also consider the exchange of a transverse-mode photon, which corresponds to the second term in the parentheses in Eq. (3.3); the term remains subdominant compared to the ELF in the range of ω that we are interested. The mCPs arriving at the detector are all highly relativistic. For ease of computation, we simply evaluate the integral at $\beta = 1$ in Eq. (3.3). For our results, we use an updated version of QCDark [68] to calculate the dielectric function [69].

The cross section for producing Q electrons is

$$\sigma_Q(\epsilon) = \int_{\omega_{\min}}^{\omega_{\max}} d\omega P_Q(\omega) \frac{d\sigma}{d\omega}(\omega, \epsilon), \quad (3.4)$$

where $\omega_{\min} = 1.1$ eV (the silicon band gap), $\omega_{\max} = 50$ eV, and $P_Q(\omega)$ is the probability that a recoil energy ω produces an event with Q electron-hole pairs. For $P_Q(\omega)$, we use the results from [70].

We plot for a silicon sensor the differential cross section $d\sigma/d\omega$ from Eq. (3.3) and also $d\sigma_Q/d\omega$ for various Q in Fig. 4, setting $\beta = 1$. We see a large peak around recoil energies of $\omega \sim 18$ eV, corresponding to $Q \sim 4e^- - 6e^-$. The reason is that relativistic mCPs can excite collective modes (plasmons) in the silicon target, enhancing the rate significantly at the “plasmon peak”, which is at $\omega \sim 18$ eV. As already discussed in [67], the fact that most events contain multiple electrons is notable, since low-threshold sensors typically have larger backgrounds (e.g., from dark current) for $Q = 1e^-$ and $2e^-$. In particular, SENSEI has demonstrated background-free searches for $Q \sim 4e^- - 6e^-$ [8].

3.3 Background estimates

As discussed in Section 3.2, the mCP signal is distinct, peaking in the $Q = 4e^- - 6e^-$ bins. In general, backgrounds can do one of two things: they can produce events that mimic the signal, or they can require various analysis cuts that reduce the effective exposure. There are four types of backgrounds that could be a concern for the mCP search: beam-induced neutrons and muons, cosmic rays, radiogenic backgrounds, and pile up from single-electron events. Whether these backgrounds are in fact a concern depends on the precise experimental setup and the specific sensors used in the readout. In particular, current Skipper-CCD sensors have very little timing information, so that it is impossible to perform an active veto of beam-induced or cosmic-ray induced backgrounds. However, a TES- or NTD-based detector, for example, will have excellent timing resolution, so that an active veto is possible. On the other hand, the high spatial resolution of the Skipper-CCDs allow one to mask pixels with high charge density, focusing on those pixels that have no or very little charge. Moreover, the proposed dual-sided CCD does have timing capabilities [71], and may be an excellent sensor for mCP searches and other searches at shallow underground sites. We here simply motivate

that a zero-background search seems plausible with low-threshold sensors after appropriate analysis cuts, but a careful study must of course be done by the proponents of a specific experiment.

We find that beam-induced backgrounds are unlikely to be a concern, as long as the shielding after the dump is sufficiently extensive. For example, the BDX collaboration has performed detailed analyses of the beam-related backgrounds in their scintillator detector. One possible concern is beam-induced neutrons, as they can be difficult to stop, but BDX finds that they are not a concern. We revisit their arguments in [Appendix C](#), and also discuss why they are unlikely to be a concern also for the low-threshold sensors envisioned in our setup.

Cosmic-ray and radiogenic backgrounds will typically deposit much larger amounts of charge than the mCPs. For example, after masking high-energy events, the SENSEI search saw no events containing $Q = 3e^- - 10e^-$ in 24 days of running at the ~ 100 m underground MINOS cavern [8]. However, the mCP search will have the sensor located at a much shallower underground site (for BDX, the detector would be located underground with an overburden of ~ 10 meter-water-equivalent). This site will have a much larger cosmic-ray muon backgrounds. For low-threshold sensors with a good timing resolution, an active veto can help to remove neutrons induced from muons interacting near the detector. For Skipper-CCDs, no active veto is possible. However several experiments are already operating Skipper-CCDs near the surface or at very shallow underground sites (including very close to nuclear reactors) to search for coherent neutrino-nucleus scattering [72–75]; moreover, recently the CONNIE and Atucha-II experiments performed a search for mCPs produced in reactor neutrinos [45]. While a background-free search seems plausible, the cosmic-ray and radiogenic backgrounds will at the very least reduce the effective exposure of the sensors to the mCP flux from the beam. In our results below, we include a 20% efficiency for this reduction in effective exposure.

Finally, low-threshold sensors sometimes suffer from large single-electron-hole backgrounds, which can originate from detector-specific “dark counts” or from secondaries produced by cosmic-ray or radiogenic backgrounds [76, 77]. Pile-up from these single-electron events can mimic events containing multiple electron-hole pairs. Fortunately, the mCP signal peaks at larger charge bins, which are difficult to produce from the pile up of multiple single-electron-hole events.

4 Results

In the parameter region that we are interested in, the mCP cross section is small and we may treat the detector as a thin target. Our observable is the number of events in a fixed set of “charge bins,” which we take to be $Q \in \{3, 4, 5, 6, 7\}$. As mentioned above, due to cosmic-ray backgrounds, we assume a 20% efficiency for a low-threshold sensor, $\epsilon_{\text{exp.}} = 0.2$, which accounts for the reduction in effective exposure. We believe this can plausibly lead to a background-free search, however a more detailed study of backgrounds will be necessary.

The expected number of signal events can therefore be written as

$$N_{\text{detected}}(\varepsilon, m_\chi) = \epsilon_{\text{exp.}} \times N_\chi^{\text{acc.}}(\varepsilon, m_\chi) \times (n_e L) \times \sum_{Q=3}^7 \sigma_Q(\varepsilon), \quad (4.1)$$

where $\epsilon_{\text{exp.}} = 0.2$ is the detector efficiency mentioned above, $L = 665 \mu\text{m}$ is the thickness of the detector, and $n_e = 6.84 \times 10^{23} \text{ cm}^{-3}$ is the number density of electrons in silicon. The accepted number of mCPs, $N_\chi^{\text{acc.}}$, includes the geometric acceptance of the detector located 20 m downstream of the target on the beam line. In [Fig. 5](#), we show the geometric efficiency for various detector areas and mCP masses. The cross section, σ_Q , per bin in Q is given in [Eq. \(3.4\)](#) (see also [Fig. 4](#)).

In the remainder of this section, we consider two mCP scenarios (a) pure millicharged particle and (b) millicharged DM that interacts with a hidden $U(1)$ gauge boson, which is kinetically mixed with ordinary photon, and discuss relevant constraints for each model. We provide the details for each model separately, including a discussion of existing constraints from the literature.

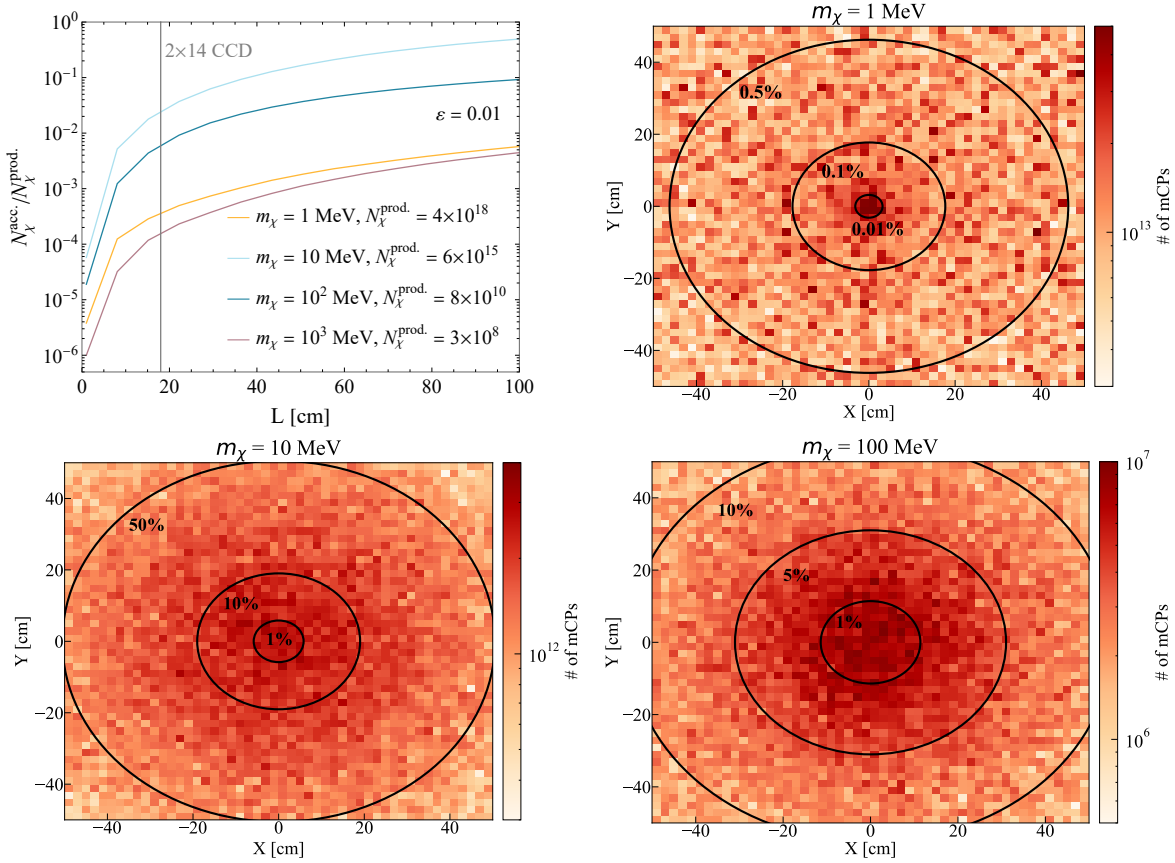


Figure 5. **Top left:** The geometric acceptance for a square detector of side length L [cm] for different mCP masses (in MeV). The curves and contours are normalized by $N_{\chi}^{\text{prod.}}$ as given in the legend. The scaling of the acceptance with particle mass can be understood by considering the different production mechanisms. The geometric acceptance from mCP annihilation increases with m_{χ} because of a decrease in transverse momentum. At higher masses, acceptance is determined by the kinematics of the parent meson, which are only moderately boosted leading to the much lower acceptance for $m_{\chi} = 1$ GeV. **Top right:** A color map that shows the number of signal events passing the X-Y plane at which the detector is located, for $\varepsilon = 0.01$ and $m_{\chi} = 1$ MeV. The contours show the accepted events as a fraction of the total produced. **Bottom left and bottom right** are as the top right figure, but for mCP masses $m_{\chi} = 10$ MeV and $m_{\chi} = 100$ MeV, respectively.

4.1 Pure millicharged particles

We first consider a “pure” mCP i.e., without any additional gauge force carrier. The simplest extension of the Standard Model of this form include a new fermion with a small hypercharge $Y = \varepsilon e$, which transforms as a singlet under $SU(2)$. This leads to a small coupling to the Z boson as well as the photon; however, constraints on the Z -coupling are always much weaker than the coupling to photons. For simplicity in what follows, we always consider a Dirac fermion, however our results are applicable up to $O(1)$ factors to any particle with a small electric charge.

In Fig. 6, we show the projected sensitivity of a Skipper-CCD detector (array) placed near the proposed BDX experiment at JLab. We include the sensitivity projections for using 1, 6, and 28 Skipper-CCD(s). These choices correspond to the minimal setup (a single 9.2×1.3 cm² Skipper-CCD), a detector array that could be readily deployed using existing detectors (6 Skipper-CCDs), and a larger square detector array

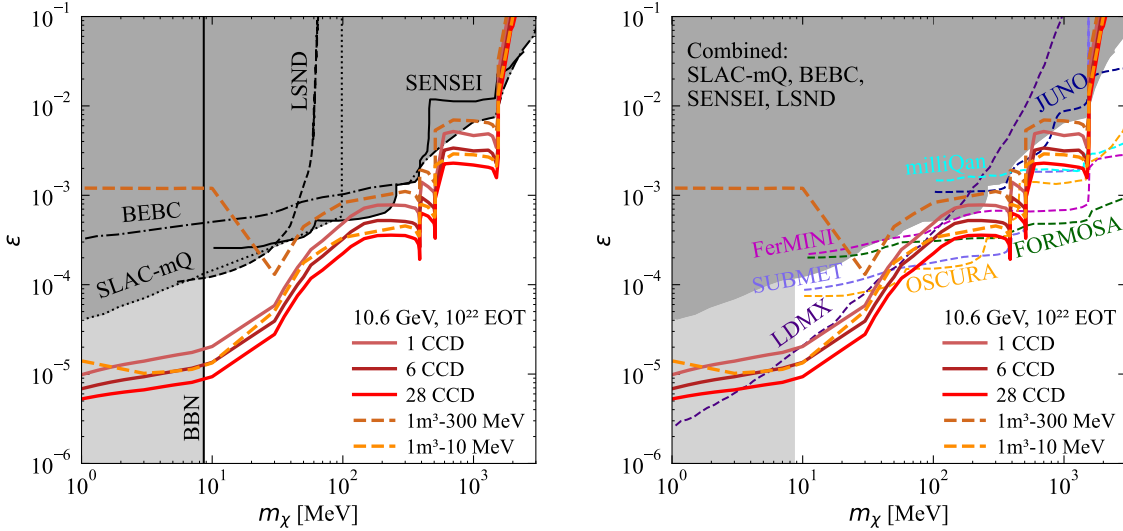


Figure 6. Pure mCP model. Left: Projected sensitivity to mCPs in the millicharge ϵ versus mCP mass m_χ plane of a Skipper-CCD detector array placed near the proposed BDX detector at Jefferson Laboratory. We assume 10^{22} electrons on target and show the sensitivity for three different low-threshold silicon detector choices (lines with various shades of red): a single 9.2×1.3 cm² Skipper-CCD, 6 Skipper-CCDs (9.2×7.8 cm²), and a larger square detector array ($\sim 18 \times 18$ cm², corresponding to 28-Skipper-CCDs). We also show two sensitivities of a hypothetical lead tungstate detector (electron number density of $n_e = 2.06 \times 10^{24}$ cm³) with volume 1 m³ and an electron-recoil energy threshold of 10 MeV and 300 MeV (two different dashed orange lines), both assumed to be background-free. The most competitive collider constraints are shown in dark gray, and the N_{eff} bound from BBN is shown in light gray. **Right:** Same as left plot, but here we show other proposed experiments in dashed curves. We call particular attention to milliQan [32] in cyan, and SUBMET [6] in lavender (which is currently taking data). Other proposed accelerator-based experiments include LDMX [78] in purple, Fermini in magenta [79], FORMOSA in green [31]. We also show the projected sensitivity of the Oscura detector [44]. The estimated sensitivity for a proposed search for cosmic ray produced mCPs in the JUNO detector [36, 38] is shown in blue.

($\sim 18 \times 18$ cm², corresponding to 28-Skipper-CCDs), respectively. We include constraints from the electron beam dump experiment at SLAC (SLAC-mQ) [2], the LSND experiment [3, 4], and proton beam dump experiments at CERN (BEBC) [39] and Fermilab (SENSEI) [8]. We also show constraints from N_{eff} that are obtained from an analysis of mCPs during Big Bang nucleosynthesis (BBN) [80, 81]. The curve for the 1 m³ detector (with a 300 MeV threshold) shown in Fig. 6 has a sharp “upturn” around $m_\chi = 20$ MeV. This occurs because, as m_χ decreases, a larger fraction of mCPs have either low E_χ or high transverse momentum. These two variables are anti-correlated in such a way that most of the flux that hits the 1 m³ detector falls below the 300 MeV threshold. A similar, albeit less stark, effect can be seen for the 10 MeV threshold curve, while the effect is non-existent for the Skipper-CCD due to its incredibly small energy threshold.

In the right-panel of Fig. 6, we include projections from proposed experiments in the literature. Of particular note is the proton beam experiment at J-PARC (SUBMET) [6], which is currently taking data, and the milliQan experiment at CERN, whose demonstrator has already produced results [32]. We also show projected sensitivity from a missing momentum search using LDMX at SLAC [78], a proposed setup using a milliQan-like detector in the Fermilab NuMI beam (FerMINI) [79], a proposed setup using a similar detector in the a proposed forward physics facility at the LHC (FORMOSA) [31], and a proposed setup using a Skipper-

CCD detector (Oscura) in the NuMI beam line [44]. Finally, beyond accelerator facilities, we also include projections from a mCP search at the Jiangmen Underground Neutrino Observatory (JUNO) [38] (see also Ref. [36]) using the mCP flux that can be produced by cosmic rays showers in the upper atmosphere [33, 36–38].

The sensitivity with a Skipper-CCD detector array in a BDX-like beam dump is competitive with essentially all proposed experiments in the ~ 10 MeV – 1 GeV mass range. Our results suggest that world-leading sensitivity can be obtained for $m_\chi \lesssim 70$ MeV, and that the electron beam setup will be competitive with the SUBMET search over their full mass-reach window. The sensitivity at low masses is dominated by the mCP flux from annihilation and trident production. Above ~ 130 MeV the flux from vector meson decays begins to dominate (the same features can be seen in the predicted SUBMET sensitivity curves).

4.2 Dark matter interacting with an ultralight dark photon

In the context of mCPs, it is interesting to explore the complementarity of accelerator-based probes of dark sectors and the direct detection of dark matter. We consider dark matter that is coupled to an ultralight dark photon that is kinetically mixed [24, 25] with the ordinary photon. Specifically, we will focus on the following low-energy effective Lagrangian

$$\mathcal{L} \supset -\frac{1}{4}\mathcal{F}_{\mu\nu}\mathcal{F}^{\mu\nu} + \frac{1}{2}m_{\mathcal{A}}^2\mathcal{A}_\mu\mathcal{A}^\mu - \frac{\kappa}{2}F_{\mu\nu}\mathcal{F}^{\mu\nu} + A_\mu J^\mu - g_D\mathcal{A}_\mu\bar{\chi}\gamma^\mu\chi, \quad (4.2)$$

where J_μ is the Standard Model electromagnetic current, $F_{\mu\nu}$ ($\mathcal{F}_{\mu\nu}$) is the field strength of the ordinary (dark) photon A_μ (\mathcal{A}_μ), and κ the kinetic mixing parameter. The mass $m_{\mathcal{A}}$ can either arise from the Stueckelberg or Higgs mechanisms. For $m_{\mathcal{A}} \ll 1$ eV, χ is very similar to an mCP. After rotating to the mass basis, the dark photon couples to J^μ (and therefore the electron bilinear $\bar{\psi}_e\gamma^\mu\psi_e$) with a coupling strength of εe , with

$$\varepsilon = \kappa g_D, \quad (4.3)$$

acting as an “effective” millicharge (even though χ does not actually have an electric charge for non-zero $m_{\mathcal{A}}$). In particular, all bounds on mCPs also apply to the χ particles.

Direct-detection searches for χ with low-threshold detectors have a distinct advantage over accelerator probes, since the scattering cross section scales as $1/q^4$, where q is the momentum transfer. Very small couplings can be probed in the future [9, 10], even those required to produce the correct relic abundance from freeze-in [9, 10, 82–84]. Current direct-detection searches already rule out a large range of couplings above the values required for freeze-in. However, for sufficiently large values, the dark-matter particles χ interact so strongly with ordinary matter that they would get stopped in the Earth’s atmosphere and crust, so that there are no direct-detection constraints [85]. For these large values, however, strong bounds from the Cosmic Microwave Background (CMB) limit the amount of dark matter to $\lesssim 0.4\%$ [86], thus restricting the χ to be a subdominant component of dark matter. It is interesting that the allowed values of ε are sufficiently large that they can be (partially) probed by accelerator-based experiments.

We note that pure mCPs may constitute the dark matter, but in the parameter region of interest for accelerator-based probes, if the dark matter were pure mCP, then (given its non-relativistic² virial velocity) it would not be able to penetrate the solar wind to intersect a terrestrial detector, and there are thus no direct-detection constraints [85, 88]. Instead, the presence of a massive dark photon screens the magnetic fields on length scales $\gg 1/m_{\mathcal{A}}$, allowing the χ to penetrate the solar wind for appropriate choices of $m_{\mathcal{A}}$. We thus focus on dark matter particles that interact with a massive, albeit ultralight, dark photon, for which there is an exciting complementarity between direct-detection and accelerator-based probes.

Accelerator probes are best understood in the plane of ε and m_χ shown in Fig. 6. These constraints can be mapped onto the direct-detection cross-section versus dark-matter mass plane, by making use of a

²We note that a pure mCP dark matter subcomponent will generate a flux with relativistic velocities from Rutherford scattering with cosmic rays, and that this flux can be enhanced by magnetic retention. This can lead to interesting and complimentary direct detection prospects [87].

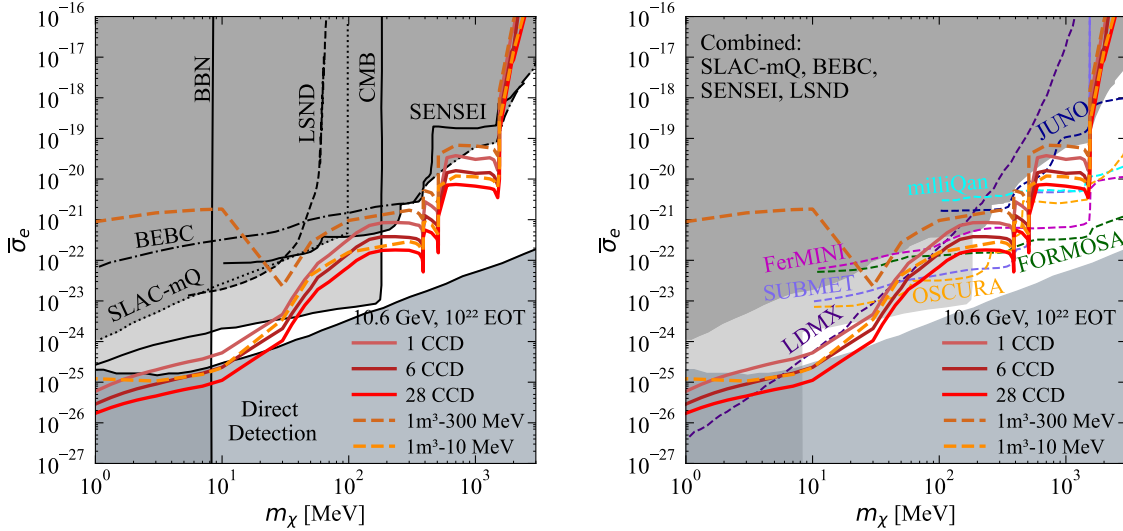


Figure 7. Dark matter interacting with an ultralight dark photon. Left: Projected sensitivity to dark matter interacting with an ultralight dark photon in the $\bar{\sigma}_e$ versus dark matter mass (m_χ) plane of a Skipper-CCD detector array placed near the proposed BDX detector at Jefferson Laboratory. We assume 10^{22} electrons on target and show the sensitivity for three different detector array choices (lines with various shades of red): a single $9.2 \times 1.3 \text{ cm}^2$ Skipper-CCD, 6 Skipper-CCDs ($9.2 \times 7.8 \text{ cm}^2$), and a larger square detector array ($\sim 18 \times 18 \text{ cm}^2$, corresponding to 28-Skipper-CCDs). We also show two sensitivities of a hypothetical lead tungstate detector (electron number density of $n_e = 2.06 \times 10^{24} \text{ cm}^3$) with volume 1 m^3 and an electron-recoil energy threshold of 10 MeV and 300 MeV (two different dashed orange lines), both assumed to be background-free. The collider constraints in dark gray and the BBN constraints in light gray are the same as in Fig. 6. The direct-detection constraints (combining all limits) are included in gray-blue [85]. We assume a dark gauge coupling of $g_D = 0.1$ and a dark-matter fractional abundance of less than 0.4%. **Right:** Same as left plot, but here we show other proposed experiments in dashed curves, as in Fig. 6.

(momentum-independent) “reference cross section”, $\bar{\sigma}_e$, defined as [9, 10]

$$\bar{\sigma}_e = \frac{16\pi\alpha^2\varepsilon^2\mu_{\chi e}^2}{(\alpha m_e)^4}, \quad (4.4)$$

where we have assumed $m_A \ll \alpha m_e$, and where $\mu_{\chi e}$ is the reduced mass of DM and electron. The actual scattering rate is proportional to $\bar{\sigma}_e \times F_{\text{DM}}^2(q)$, where the dark-matter form factor ($F_{\text{DM}} = (\alpha m_e/q)^2$) captures the momentum-dependence of the scattering.

In Fig. 7, we include all of the previous pure mCP constraints and projections, now in terms of the reference cross section $\bar{\sigma}_e$. We assume the χ ’s constitute much less than 0.4% of the dark-matter abundance, which avoids the very strong CMB constraints that arise from the χ scattering off ordinary matter in the early Universe [86]. We also include combined direct detection constraints from SENSEI, CDMS-HVeV, XENON10, XENON100, DarkSide-50 experiments [11, 14, 19, 21, 89, 90] with the compiled limits take from [85], whose upper boundary is insensitive to the precise value of the dark matter abundance. We do not show bounds that are sensitive to the precise abundance, e.g. [91–93]. These constraints are superimposed on the accelerator and BBN constraints discussed in Fig. 6, which are applicable independent of the model assumptions related to, e.g., the fraction of dark matter or the mass of the light-mediator. In addition, the presence of a low-mass dark photon in the model is constrained by the CMB bounds on the effective number of relativistic degrees of freedom, N_{eff} ; we choose the most conservative bound, which arises for relatively large values of the dark

gauge coupling (e.g., $g_D = 0.1$) [81, 85, 94, 95]. We see that the BDX-like setup we study in this paper is capable of probing a large fraction of the open window.

5 Discussion and Conclusions

In this work, we have demonstrated that a high-intensity, medium-energy electron beam dump together with an ultralow-threshold sensor offers world-leading sensitivity to mCPs. Searching for low-mass dark sectors at accelerator facilities is now widely appreciated as a complimentary method by which to probe a variety of dark-sector models that have interesting and non-trivial cosmological histories. Models with a mCP in their spectrum represent a minimal example of such a scenario and are unique in that their detection signature benefits from ultralow thresholds. Since these ultralow threshold detectors are small (e.g., gram-scale) they can be easily deployed.

In our paper, for concreteness, we have performed a detailed study of mCP production in the aluminum target planned for the Beam Dump eXperiment (BDX) at J-Lab. We find that a number of previously overlooked production modes (namely e^+e^- annihilation and vector-meson photoproduction) substantially increase the sensitivity of electron beam dumps to mCPs and likely to dark sectors more generally. Our findings suggest that the SLAC-mQ exclusions may be underestimated, and suggest that a reanalysis of their model for mCP production in the target is worth revisiting.

Looking forward, our study further motivates the inclusion of small ultralow-threshold sensors in future beam-dump and collider facilities. Although we have focussed on electron beam dumps a small Skipper-CCD array like the ones discussed above could be easily included in facilities such as SHiP, the LHC’s forward physics facility, or in the DUNE near-detector complex. We encourage further exploration of ultralow-threshold detectors in beam-dump experiments [26, 96–99] and in the forward region of colliders such as the LHC [31, 32, 100–103].

Acknowledgments

We thank Duncan Adams for helpful conversations related to neutron backgrounds, Marco Battaglieri for helpful correspondence about the BDX detector, Christopher Hill for correspondences on the SUBMET experiment, Javier Tiffenberg for useful comments on CCD readout and cosmic-ray induced backgrounds, and Kevin Zhou for helpful discussions about vector meson photoproduction. RE acknowledges support from DOE Grant DE-SC0009854, Simons Investigator in Physics Award 623940, Heising-Simons Foundation Grant No. 79921, Binational Science Foundation Grant No. 2020220. MD and HX are supported in part by DOE Grant DE-SC0009854 and Simons Investigator in Physics Award 623940. In addition, HX is supported in part by the Binational Science Foundation Grant No. 2020220. PL and ZL are supported in part by the DOE Grant No. DE-SC0011842 and a Sloan Research Fellowship from the Alfred P. Sloan Foundation at the University of Minnesota. RP is supported by the Neutrino Theory Network under Award Number DEAC02-07CH11359, the U.S. Department of Energy, Office of Science, Office of High Energy Physics under Award Number DE-SC0011632, and by the Walter Burke Institute for Theoretical Physics.

A Dependence of electromagnetic shower simulation on energy threshold

When simulating particle production in an electromagnetic cascade one must supply a prescription for when to halt the numerical simulation of the cascade. In PETITE this is done using a minimum energy threshold. In this appendix, we show how the predicted fluxes arriving at the Skipper-CCD converge as a function of the minimum energy threshold. We will explicitly see that our results are not sensitive to variations in the minimum energy threshold.

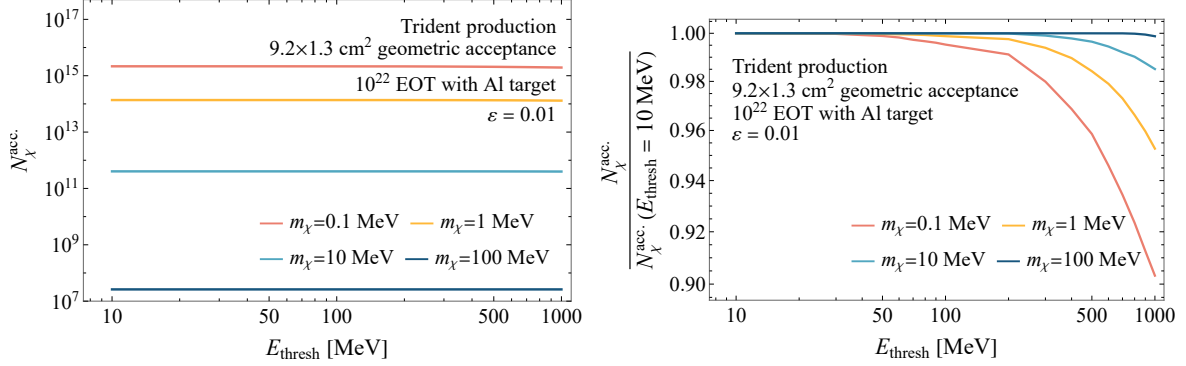


Figure 8. **Left:** The number of mCPs produced in trident processes in the EM shower that pass through a detector of area $9.2 \times 1.3 \text{ cm}^2$ located 20 m downstream of the target ($N_{\chi}^{\text{acc.}}$) as a function of the shower energy threshold, for a millicharge of $\varepsilon = 0.01$. **Right:** The ratio of $N_{\chi}^{\text{acc.}}$ to $N_{\chi}^{\text{acc.}}(E_{\text{thresh}} = 10 \text{ MeV})$, the accepted number of mCPs evaluated at a shower energy threshold of 10 MeV. We see that for $E_{\text{thresh}} \lesssim 50 \text{ MeV}$ the flux hitting the detector is insensitive to the shower threshold.

A.1 Trident production

In Fig. 8 (left), we show the number of mCPs produced in trident processes in the EM shower that pass through a detector of area $9.2 \text{ cm} \times 1.3 \text{ cm}$ located 20 m downstream of the target ($N_{\chi}^{\text{acc.}}$) versus the energy threshold. In the right plot, we show the ratio of $N_{\chi}^{\text{acc.}}$ to the accepted number of mCP evaluated at a shower energy threshold of 10 MeV, denoted $N_{\chi}^{\text{acc.}}(E_{\text{thresh}} = 10 \text{ MeV})$. For low-mass mCPs (e.g., $m_{\chi} = 0.1 \text{ MeV}$), the accepted number of mCPs from trident production increases by about 10% from lowering the energy threshold from 1 GeV to 50 MeV, and remains flat for even lower energy threshold values. Although the number of low-mass mCPs produced increases for lower energy thresholds, most of them will not go through the small downstream detector area. For heavier mCPs, such as for $m_{\chi} = 100 \text{ MeV}$, an energy threshold of 1 GeV is already sufficiently low to properly estimate the number of mCPs that pass through the detector. The reason is that the majority of secondary particles do not have enough energy to produce heavy mCPs, and those that do, will typically produce them at large angles. In any case, we see here that an energy threshold of $E_{\text{thresh}} = 10 \text{ MeV}$ is more than sufficient for robustly estimating the number of mCPs produced through trident processes in the EM shower.

A.2 Annihilation production

The annihilation process dominates the mCP flux arriving at the detector in the $2 \text{ MeV} \lesssim m_{\chi} \lesssim 50 \text{ MeV}$ window (see right panel of Fig. 3). In Fig. 9, we show that an energy threshold of 10 MeV is sufficient to reliably estimate all the mCPs produced from secondary particles in the EM shower, which pass through the downstream detector area of mCP masses between 5 and 50 MeV. The kinematic threshold for producing mCPs with mass $m_{\chi} = 5 \text{ MeV}$ is 100 MeV; hence, the results are independent of any threshold choice below 100 MeV. For much lower m_{χ} , although the kinematic threshold is lower, the mCPs produced from low-energy positron will have a wider angular distribution and will not pass through the downstream detector. Moreover, as shown in the right panel of Fig. 3, the annihilation process is not competitive to the trident process in the low mass region, so that a 10 MeV threshold is sufficiently low also to estimate the mCPs produced in electron-positron annihilation. Similar conclusions hold for the Compton production, which in any case is subdominant.

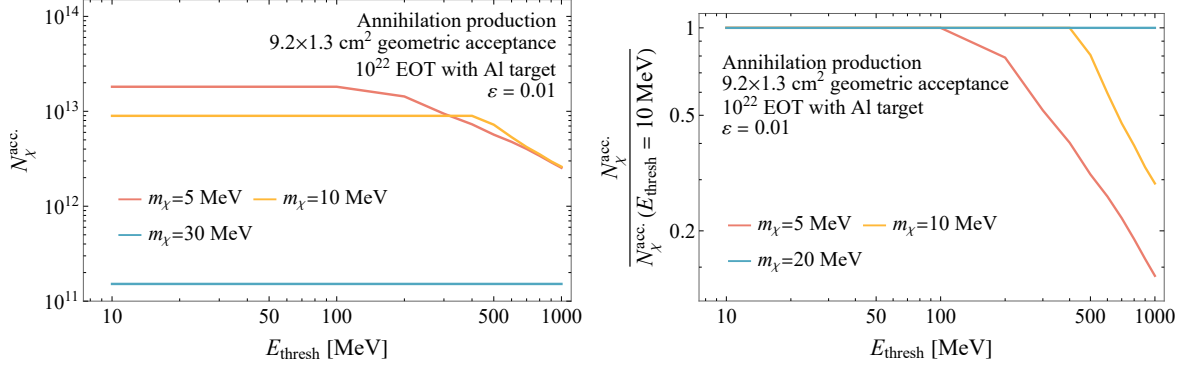


Figure 9. **Left:** The number of mCPs produced in electron-positron annihilation in the EM shower that pass through a detector of area $9.2 \times 1.3 \text{ cm}^2$ located 20 m downstream of the target ($N_{\chi}^{\text{acc.}}$) versus the energy threshold, for a millicharge of $\varepsilon = 0.01$. **Right:** The ratio of $N_{\chi}^{\text{acc.}}$ to $N_{\chi}^{\text{acc.}}(E_{\text{thresh}} = 10 \text{ MeV})$, the accepted number of mCPs evaluated at a shower energy threshold of 10 MeV. We see that for $E_{\text{thresh}} \lesssim 100 \text{ MeV}$, the flux hitting the detector is insensitive to the shower threshold.

B Multiple scattering

From the beam-dump to the well where the detector is located, there is 5.4 m of concrete and 14.2 m of dirt [63]. When mCP particles pass through this material, they can be deflected by multiple small-angle Coulomb scatters. The theory of multiple Coulomb scattering is well developed, and the core of the distribution in scattering angle can be well modeled by a Gaussian distribution with a root-mean-squared (RMS) width given by [55],

$$\theta_0 = \frac{13.6 \text{ MeV}}{\beta p_{\chi}} \varepsilon \sqrt{\frac{x}{X_0}} \left(1 + 0.088 \log_{10} \left(\frac{x \varepsilon^2}{X_0 \beta^2} \right) \right), \quad (\text{B.1})$$

where β is the velocity, p_{χ} is the momentum of the mCP particle from the beam dump, ε is its millicharge, x is the thickness of the medium, and X_0 is the medium's radiation length. The radiation length of concrete is 11.55 cm [104]. We model the dirt as standard rock (with radiation length of 26.54 g/cm^2 [105]), accounting for the decreased density of dirt (1.7 g/cm^3 for dirt [42] vs 2.7 g/cm^3 for standard rock), and we obtain $X_0 = 15.9 \text{ cm}$ for the dirt. We add the RMS deflecting angle from concrete and dirt in quadrature for the total result, since both materials are homogeneous and appear in series.

To study the impact on detection prospects with a Skipper-CCD, we compute the transverse distance of the particles on the plane of detector (located 20 m away) caused by scatterings in the concrete and dirt using $\Delta d = \theta_0 \times 20 \text{ m}$. The deflection depends on the millicharge and momentum of the mCP (we assume $\beta = 1$, which is very accurate for $m_{\chi} \lesssim 1 \text{ GeV}$). We plot our results as a function of p_{χ} for different values of millicharge in Fig. 10. One immediately sees that the deflection by the dirt and concrete is not experimentally significant for $\varepsilon \lesssim 10^{-2}$. This region of (relatively large) ε is already robustly excluded by existing experiments as can be seen in Fig. 6. We therefore conclude that the multiple scatterings in the medium does not have a significant impact on our projected sensitivity, except for the regions of large ε that are already excluded by existing searches.

C Beam-induced neutron backgrounds

The BDX collaboration studied beam-related and cosmic-ray backgrounds for the proposed BDX-DRIFT-1m and BDX-DRIFT-10m detectors (this is distinct from the proposed BDX PbWO_4 detector), concluding that a zero-background experiment is possible with an active veto system [41, 106]. In particular, background particles such as neutrinos, muons, neutrons, and photons were simulated using GEANT4 with threshold energies of 10 MeV. However, a Skipper-CCD detector will (a) not have an active veto system and (b) has

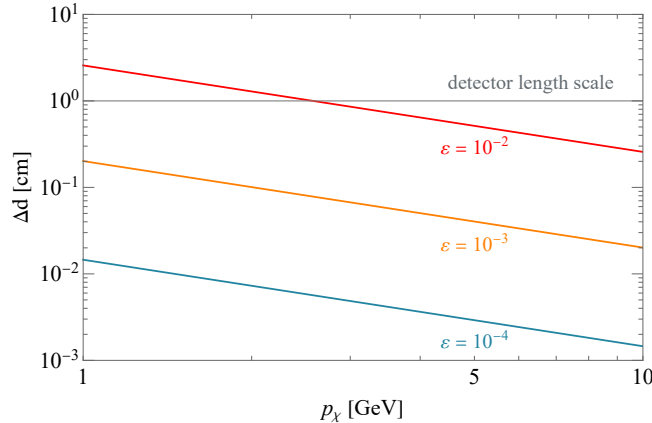


Figure 10. The deflected distance from multiple scattering on the plane of a detector located 20 m from the beam dump (after traversing 5.4 m of concrete and 14.2 m of dirt) as a function of mCP momentum, p_χ , for different millicharges, ε . A minimum detector length scale of 1 cm is marked as the gray line. We see that for the values of ε that are not presently excluded, multiple Coulomb scattering does not affect the sensitivity projections computed in the main text.

an energy threshold of $O(\text{eV})$ compared to the higher thresholds for the BDX-DRIFT design. Therefore, it is important to carefully re-consider background particles, which may have energies that are undetectable in the proposed BDX experiment and were thus not simulated in their studies.

In general, particles with energy of $O(\text{MeV})$ will deposit large amount of charge in the Skipper-CCD detector (much more than the few electron-hole pairs from mCPs), which can be masked. Cosmic-ray background as well as beam-induced neutrinos, muons, and photons will all be highly energetic, and therefore these events can be easily rejected. As discussed in [Section 3.3](#), the required masking of high-energy backgrounds will decrease the effective exposure, which we include as an efficiency factor in our final sensitivity estimates. In the remainder of this appendix, we will discuss beam-induced neutrons that reach the detector, since these have been estimated by BDX. (Note that cosmic-ray-induced neutrons near the detector are likely a larger concern and require careful study by the proponents of a particular experiment, as they depend sensitively on the precise detector technology being used.)

There are two categories of beam-related neutrons that naively may contribute as a background: beam-induced neutrons produced from the electron interactions, and beam-induced muons that interact with the 10 m iron absorber (located along the beam line in between the concrete target area and the detector area) and that produces spallation neutrons. Neutrons as well as other muon secondaries are considered in [\[41\]](#), albeit with a discussion that assumes the BDX energy thresholds.

The recoil energy of a nucleus after an elastic neutron-nucleus scatter (assuming non-relativistic kinematics) is given by

$$T_{A,\text{rec}} = \frac{4 T_n m_n m_A \sin^2\left(\frac{\theta}{2}\right)}{(m_n + m_A)^2}, \quad (\text{C.1})$$

where $T_{A,\text{rec}}$ is the kinetic energy of the final state nucleus, m_n (m_A) is the neutron (nucleus) mass, θ is the scattering angle in the lab-frame, and T_n is the incoming neutron kinetic energy. In order for a neutron to deposit an ionization energy that could fake a mCP event, it would need to produce 4-7 electron-hole pairs, which corresponds to a narrow range of $T_{A,\text{rec}}$; the precise range is uncertain due to the uncertainty in the ionization yield of low-energy nuclear recoils, but it (very) roughly corresponds to 150 to 400 eV [\[107–109\]](#). The relevant neutron energies that can produce such $T_{A,\text{rec}}$ depends sensitively on θ , but can be as low as ~ 1 keV as can be checked explicitly using [Eq. \(C.1\)](#).

The BDX collaboration estimates that for 10^{22} EOT, about 290 neutrons scatter in their proposed BDX-DRIFT-10 m detector, which has a volume of $1 \text{ m} \times 1 \text{ m} \times 10 \text{ m}$ [106]. The ultralow-threshold sensors would be significantly smaller in size, so that the number of neutrons that pass through the sensor is significantly smaller; for example, naively extrapolating the BDX-DRIFT-10 m detector area in line with the beam (1 m^2) to the area of a single Skipper-CCD that is in line with the beam ($\sim 12 \text{ cm}^2$) suggests that the number of neutrons that pass through the Skipper-CCD sensor is < 1 . In addition, even if it scatters, the probability of producing $Q = 3e^- - 7e^-$ is low.

Finally, we consider spallation neutron backgrounds from beam-induced muon interactions in the iron absorber. The BDX collaboration considered beam-induced muon secondaries and carefully simulates neutron production from muons three times with increased statistics [41]. It is concluded that neutron secondaries are a negligible background if the detector is placed 20 meters from the beam dump. This conclusion holds for both the nominal BDX detector and the smaller ultralow-threshold detectors we have proposed in this work.

References

- [1] J. D. Bjorken, R. Essig, P. Schuster, and N. Toro, “New Fixed-Target Experiments to Search for Dark Gauge Forces,” *Phys. Rev. D* **80** (2009) 075018, [arXiv:0906.0580 \[hep-ph\]](#).
- [2] A. A. Prinz *et al.*, “Search for millicharged particles at SLAC,” *Phys. Rev. Lett.* **81** (1998) 1175–1178, [arXiv:hep-ex/9804008](#).
- [3] **LSND** Collaboration, L. B. Auerbach *et al.*, “Measurement of electron - neutrino - electron elastic scattering,” *Phys. Rev. D* **63** (2001) 112001, [arXiv:hep-ex/0101039](#).
- [4] G. Magill, R. Plestid, M. Pospelov, and Y.-D. Tsai, “Millicharged particles in neutrino experiments,” *Phys. Rev. Lett.* **122** (2019) no. 7, 071801, [arXiv:1806.03310 \[hep-ph\]](#).
- [5] Y. Kahn, G. Krnjaic, J. Thaler, and M. Toups, “DAEδALUS and dark matter detection,” *Phys. Rev. D* **91** (2015) no. 5, 055006, [arXiv:1411.1055 \[hep-ph\]](#).
- [6] J. H. Kim, I. S. Hwang, and J. H. Yoo, “Search for sub-millicharged particles at J-PARC,” *JHEP* **05** (2021) 031, [arXiv:2102.11493 \[hep-ex\]](#).
- [7] C. A. Argüelles *et al.*, “New opportunities at the next-generation neutrino experiments I: BSM neutrino physics and dark matter,” *Rept. Prog. Phys.* **83** (2020) no. 12, 124201, [arXiv:1907.08311 \[hep-ph\]](#).
- [8] **SENSEI** Collaboration, L. Barak *et al.*, “SENSEI: Search for Millicharged Particles produced in the NuMI Beam,” [arXiv:2305.04964 \[hep-ex\]](#).
- [9] R. Essig, J. Mardon, and T. Volansky, “Direct Detection of Sub-GeV Dark Matter,” *Phys. Rev.* **D85** (2012) 076007, [arXiv:1108.5383 \[hep-ph\]](#).
- [10] R. Essig, M. Fernandez-Serra, J. Mardon, A. Soto, T. Volansky, and T.-T. Yu, “Direct Detection of sub-GeV Dark Matter with Semiconductor Targets,” *JHEP* **05** (2016) 046, [arXiv:1509.01598 \[hep-ph\]](#).
- [11] **SENSEI** Collaboration, M. Crisler, R. Essig, J. Estrada, G. Fernandez, J. Tiffenberg, M. Sofio haro, T. Volansky, and T.-T. Yu, “SENSEI: First Direct-Detection Constraints on sub-GeV Dark Matter from a Surface Run,” *Phys. Rev. Lett.* **121** (2018) no. 6, 061803, [arXiv:1804.00088 \[hep-ex\]](#).
- [12] **SENSEI** Collaboration, O. Abramoff *et al.*, “SENSEI: Direct-Detection Constraints on Sub-GeV Dark Matter from a Shallow Underground Run Using a Prototype Skipper-CCD,” *Phys. Rev. Lett.* **122** (2019) no. 16, 161801, [arXiv:1901.10478 \[hep-ex\]](#).
- [13] **SENSEI** Collaboration, L. Barak *et al.*, “SENSEI: Direct-Detection Results on sub-GeV Dark Matter from a New Skipper-CCD,” *Phys. Rev. Lett.* **125** (2020) no. 17, 171802, [arXiv:2004.11378 \[astro-ph.CO\]](#).

- [14] **DarkSide** Collaboration, P. Agnes *et al.*, “Constraints on Sub-GeV Dark-Matter–Electron Scattering from the DarkSide-50 Experiment,” *Phys. Rev. Lett.* **121** (2018) no. 11, 111303, [arXiv:1802.06998 \[astro-ph.CO\]](#).
- [15] **DarkSide** Collaboration, P. Agnes *et al.*, “Search for Dark Matter Particle Interactions with Electron Final States with DarkSide-50,” *Phys. Rev. Lett.* **130** (2023) no. 10, 101002, [arXiv:2207.11968 \[hep-ex\]](#).
- [16] **FUNK Experiment** Collaboration, A. Andrianavalomahefa *et al.*, “Limits from the Funk Experiment on the Mixing Strength of Hidden-Photon Dark Matter in the Visible and Near-Ultraviolet Wavelength Range,” *Phys. Rev. D* **102** (2020) no. 4, 042001, [arXiv:2003.13144 \[astro-ph.CO\]](#).
- [17] **DAMIC** Collaboration, A. Aguilar-Arevalo *et al.*, “Constraints on Light Dark Matter Particles Interacting with Electrons from DAMIC at SNOLAB,” *Phys. Rev. Lett.* **123** (2019) no. 18, 181802, [arXiv:1907.12628 \[astro-ph.CO\]](#).
- [18] **XENON** Collaboration, E. Aprile *et al.*, “Light Dark Matter Search with Ionization Signals in XENON1T,” *Phys. Rev. Lett.* **123** (2019) no. 25, 251801, [arXiv:1907.11485 \[hep-ex\]](#).
- [19] R. Essig, T. Volansky, and T.-T. Yu, “New Constraints and Prospects for sub-GeV Dark Matter Scattering off Electrons in Xenon,” *Phys. Rev. D* **96** (2017) no. 4, 043017, [arXiv:1703.00910 \[hep-ph\]](#).
- [20] **EDELWEISS** Collaboration, Q. Arnaud *et al.*, “First germanium-based constraints on sub-MeV Dark Matter with the EDELWEISS experiment,” *Phys. Rev. Lett.* **125** (2020) no. 14, 141301, [arXiv:2003.01046 \[astro-ph.GA\]](#).
- [21] **SuperCDMS** Collaboration, R. Agnese *et al.*, “First Dark Matter Constraints from a SuperCDMS Single-Charge Sensitive Detector,” *Phys. Rev. Lett.* **121** (2018) no. 5, 051301, [arXiv:1804.10697 \[hep-ex\]](#). [Erratum: *Phys.Rev.Lett.* 122, 069901 (2019)].
- [22] L. B. Okun, M. B. Voloshin, and V. I. Zakharov, “Electrical Neutrality of Atoms and Grand Unification Models,” *Phys. Lett. B* **138** (1984) 115–120.
- [23] D. E. Brahm and L. J. Hall, “U(1)-prime Dark Matter,” *Phys. Rev. D* **41** (1990) 1067.
- [24] B. Holdom, “Two U(1)’s and Epsilon Charge Shifts,” *Phys. Lett. B* **166** (1986) 196–198.
- [25] P. Galison and A. Manohar, “Two Z ’s or not two Z ’s?,” *Phys. Lett. B* **136** (1984) 279–283.
- [26] **SBND** Collaboration, S. Balasubramanian, “Beyond the Standard Model New Physics Searches with SBND †,” *Phys. Sci. Forum* **8** (2023) no. 1, 68.
- [27] R. Harnik, Z. Liu, and O. Palamara, “Millicharged Particles in Liquid Argon Neutrino Experiments,” *JHEP* **07** (2019) 170, [arXiv:1902.03246 \[hep-ph\]](#).
- [28] **ArgoNeuT** Collaboration, R. Acciarri *et al.*, “Improved Limits on Millicharged Particles Using the ArgoNeuT Experiment at Fermilab,” *Phys. Rev. Lett.* **124** (2020) no. 13, 131801, [arXiv:1911.07996 \[hep-ex\]](#).
- [29] **CMS** Collaboration, S. Chatrchyan *et al.*, “Search for Fractionally Charged Particles in pp Collisions at $\sqrt{s} = 7$ TeV,” *Phys. Rev. D* **87** (2013) no. 9, 092008, [arXiv:1210.2311 \[hep-ex\]](#). [Erratum: *Phys.Rev.D* 106, 099903 (2022)].
- [30] A. Haas, C. S. Hill, E. Izaguirre, and I. Yavin, “Looking for milli-charged particles with a new experiment at the LHC,” *Phys. Lett. B* **746** (2015) 117–120, [arXiv:1410.6816 \[hep-ph\]](#).
- [31] S. Foughi-Abari, F. Kling, and Y.-D. Tsai, “Looking forward to millicharged dark sectors at the LHC,” *Phys. Rev. D* **104** (2021) no. 3, 035014, [arXiv:2010.07941 \[hep-ph\]](#).

- [32] **milliQan** Collaboration, A. Ball *et al.*, “Sensitivity to millicharged particles in future proton-proton collisions at the LHC with the milliQan detector,” *Phys. Rev. D* **104** (2021) no. 3, 032002, [arXiv:2104.07151 \[hep-ex\]](#).
- [33] R. Plestid, V. Takhistov, Y.-D. Tsai, T. Bringmann, A. Kusenko, and M. Pospelov, “New Constraints on Millicharged Particles from Cosmic-ray Production,” *Phys. Rev. D* **102** (2020) 115032, [arXiv:2002.11732 \[hep-ph\]](#).
- [34] **MACRO** Collaboration, M. Ambrosio *et al.*, “A Search for lightly ionizing particles with the MACRO detector,” *Phys. Rev. D* **62** (2000) 052003, [arXiv:hep-ex/0002029](#).
- [35] **Majorana** Collaboration, S. I. Alvis *et al.*, “First Limit on the Direct Detection of Lightly Ionizing Particles for Electric Charge as Low as $e/1000$ with the Majorana Demonstrator,” *Phys. Rev. Lett.* **120** (2018) no. 21, 211804, [arXiv:1801.10145 \[hep-ex\]](#).
- [36] C. A. Argüelles Delgado, K. J. Kelly, and V. Muñoz Alborno, “Millicharged particles from the heavens: single- and multiple-scattering signatures,” *JHEP* **11** (2021) 099, [arXiv:2104.13924 \[hep-ph\]](#).
- [37] M. Du, R. Fang, and Z. Liu, “Millicharged particles from proton bremsstrahlung in the atmosphere,” [arXiv:2211.11469 \[hep-ph\]](#).
- [38] H. Wu, E. Hardy, and N. Song, “Searching for heavy millicharged particles from the atmosphere,” [arXiv:2406.01668 \[hep-ph\]](#).
- [39] G. Marocco and S. Sarkar, “Blast from the past: Constraints on the dark sector from the BEBC WA66 beam dump experiment,” *SciPost Phys.* **10** (2021) no. 2, 043, [arXiv:2011.08153 \[hep-ph\]](#).
- [40] **BDX** Collaboration, M. Battaglieri *et al.*, “Dark matter search in a Beam-Dump eXperiment (BDX) at Jefferson Lab,” [arXiv:1406.3028 \[physics.ins-det\]](#).
- [41] **BDX** Collaboration, M. Battaglieri *et al.*, “Dark Matter Search in a Beam-Dump eXperiment (BDX) at Jefferson Lab,” [arXiv:1607.01390 \[hep-ex\]](#).
- [42] **BDX** Collaboration, M. Battaglieri *et al.*, “Dark matter search in a Beam-Dump eXperiment (BDX) at Jefferson Lab: an update on PR12-16-001,” [arXiv:1712.01518 \[physics.ins-det\]](#).
- [43] **BDX** Collaboration, M. Battaglieri *et al.*, “Dark Matter Search in a Beam-Dump EXperiment (BDX) at Jefferson Lab – 2018 Update to PR12-16-001,” [arXiv:1910.03532 \[physics.ins-det\]](#).
- [44] **Oscura** Collaboration, S. Perez *et al.*, “Early Science with the Oscura Integration Test,” [arXiv:2304.08625 \[hep-ex\]](#).
- [45] **CONNIE, Atucha-II** Collaboration, A. A. Aguilar-Arevalo *et al.*, “Search for reactor-produced millicharged particles with Skipper-CCDs at the CONNIE and Atucha-II experiments,” [arXiv:2405.16316 \[hep-ex\]](#).
- [46] **SuperCDMS** Collaboration, D. W. Amaral *et al.*, “Constraints on low-mass, relic dark matter candidates from a surface-operated SuperCDMS single-charge sensitive detector,” *Phys. Rev. D* **102** (2020) no. 9, 091101, [arXiv:2005.14067 \[hep-ex\]](#).
- [47] **SuperCDMS** Collaboration, M. F. Albakry *et al.*, “Light Dark Matter Constraints from SuperCDMS HVeV Detectors Operated Underground with an Anticoincidence Event Selection,” [arXiv:2407.08085 \[hep-ex\]](#).
- [48] J. Alwall, R. Frederix, S. Frixione, V. Hirschi, F. Maltoni, O. Mattelaer, H. S. Shao, T. Stelzer, P. Torrielli, and M. Zaro, “The automated computation of tree-level and next-to-leading order differential cross sections, and their matching to parton shower simulations,” *JHEP* **07** (2014) 079, [arXiv:1405.0301 \[hep-ph\]](#).

- [49] A. Alloul, N. D. Christensen, C. Degrande, C. Duhr, and B. Fuks, “FeynRules 2.0 - A complete toolbox for tree-level phenomenology,” *Comput. Phys. Commun.* **185** (2014) 2250–2300, [arXiv:1310.1921 \[hep-ph\]](#).
- [50] A. Celentano, L. Darmé, L. Marsicano, and E. Nardi, “New production channels for light dark matter in hadronic showers,” *Phys. Rev. D* **102** (2020) no. 7, 075026, [arXiv:2006.09419 \[hep-ph\]](#).
- [51] K. J. Kim and Y.-S. Tsai, “Improved Weizsacker-William Method and its Application to Lepton and W Boson Pair Production,” *Phys. Rev. D* **8** (1973) 3109.
- [52] Y.-S. Tsai, “Pair Production and Bremsstrahlung of Charged Leptons,” *Rev. Mod. Phys.* **46** (1974) 815. [Erratum: *Rev.Mod.Phys.* 49, 421–423 (1977)].
- [53] M. D. Diamond and P. Schuster, “Searching for Light Dark Matter with the SLAC Millicharge Experiment,” *Phys. Rev. Lett.* **111** (2013) no. 22, 221803, [arXiv:1307.6861 \[hep-ph\]](#).
- [54] X. Chu, J. Pradler, and L. Semmelrock, “Light dark states with electromagnetic form factors,” *Phys. Rev. D* **99** (2019) no. 1, 015040, [arXiv:1811.04095 \[hep-ph\]](#).
- [55] **Particle Data Group** Collaboration, S. Navas *et al.*, “Review of particle physics,” *Phys. Rev. D* **110** (2024) no. 3, 030001.
- [56] N. Blinov, P. J. Fox, K. J. Kelly, P. A. N. Machado, and R. Plestid, “Dark fluxes from electromagnetic cascades,” *JHEP* **07** (2024) 022, [arXiv:2401.06843 \[hep-ph\]](#).
- [57] Y.-S. Liu and G. A. Miller, “Validity of the Weizsäcker-Williams approximation and the analysis of beam dump experiments: Production of an axion, a dark photon, or a new axial-vector boson,” *Phys. Rev. D* **96** (2017) no. 1, 016004, [arXiv:1705.01633 \[hep-ph\]](#).
- [58] S. N. Gninenko, D. V. Kirpichnikov, and N. V. Krasnikov, “Probing millicharged particles with NA64 experiment at CERN,” *Phys. Rev. D* **100** (2019) no. 3, 035003, [arXiv:1810.06856 \[hep-ph\]](#).
- [59] P. Schuster, N. Toro, and K. Zhou, “Probing invisible vector meson decays with the NA64 and LDMX experiments,” *Phys. Rev. D* **105** (2022) no. 3, 035036, [arXiv:2112.02104 \[hep-ph\]](#).
- [60] Y.-S. Tsai and V. Whitis, “Thick Target Bremsstrahlung and Target Consideration for Secondary Particle Production by Electrons,” *Phys. Rev.* **149** (1966) 1248–1257.
- [61] J. M. Laget, “Photoproduction of vector mesons at large transfer,” *Phys. Lett. B* **489** (2000) 313–318, [arXiv:hep-ph/0003213](#).
- [62] **GlueX** Collaboration, S. Adhikari *et al.*, “Measurement of the J/ψ photoproduction cross section over the full near-threshold kinematic region,” *Phys. Rev. C* **108** (2023) no. 2, 025201, [arXiv:2304.03845 \[nucl-ex\]](#).
- [63] M. Battaglieri *et al.*, “The BDX-MINI detector for Light Dark Matter search at JLab,” *Eur. Phys. J. C* **81** (2021) no. 2, 164, [arXiv:2011.10532 \[physics.ins-det\]](#).
- [64] B. Batell, R. Essig, and Z. Surujon, “Strong Constraints on Sub-GeV Dark Sectors from SLAC Beam Dump E137,” *Phys. Rev. Lett.* **113** (2014) no. 17, 171802, [arXiv:1406.2698 \[hep-ph\]](#).
- [65] M. Battaglieri *et al.*, “Dark matter search with the BDX-MINI experiment,” *Phys. Rev. D* **106** (2022) no. 7, 072011, [arXiv:2208.01387 \[hep-ex\]](#).
- [66] **SENSEI** Collaboration, J. Tiffenberg, M. Sofo-Haro, A. Drlica-Wagner, R. Essig, Y. Guardincerri, S. Holland, T. Volansky, and T.-T. Yu, “Single-electron and single-photon sensitivity with a silicon Skipper CCD,” *Phys. Rev. Lett.* **119** (2017) no. 13, 131802, [arXiv:1706.00028 \[physics.ins-det\]](#).
- [67] R. Essig, R. Plestid, and A. Singal, “Collective excitations and low-energy ionization signatures of relativistic particles in silicon detectors,” [arXiv:2403.00123 \[hep-ph\]](#).

- [68] C. E. Dreyer, R. Essig, M. Fernandez-Serra, A. Singal, and C. Zhen, “Fully ab-initio all-electron calculation of dark matter-electron scattering in crystals with evaluation of systematic uncertainties,” *Phys. Rev. D* **109** (2024) no. 11, 115008, [arXiv:2306.14944 \[hep-ph\]](#).
- [69] C. E. Dreyer, R. Essig, M. Fernandez-Serra, M. Hott, and A. Singal, *in progress*.
- [70] K. Ramanathan and N. Kurinsky, “Ionization yield in silicon for eV-scale electron-recoil processes,” *Phys. Rev. D* **102** (2020) no. 6, 063026, [arXiv:2004.10709 \[astro-ph.IM\]](#).
- [71] J. Tiffenberg, D. Egaña Ugrinovic, M. Sofo Haro, P. Du, R. Essig, G. Fernandez-Moroni, and S. Uemura, “Dual-sided charge-coupled devices,” *Phys. Rev. Applied* **22** (2024) no. 1, 014008, [arXiv:2307.13723 \[physics.ins-det\]](#).
- [72] **CONNIE** Collaboration, A. A. Aguilar-Arevalo *et al.*, “Searches for CE ν NS and Physics beyond the Standard Model using Skipper-CCDs at CONNIE,” [arXiv:2403.15976 \[hep-ex\]](#).
- [73] **CONNIE** Collaboration, A. Aguilar-Arevalo *et al.*, “Search for coherent elastic neutrino-nucleus scattering at a nuclear reactor with CONNIE 2019 data,” *JHEP* **05** (2022) 017, [arXiv:2110.13033 \[hep-ex\]](#).
- [74] **CONNIE** Collaboration, A. Aguilar-Arevalo *et al.*, “Exploring low-energy neutrino physics with the Coherent Neutrino Nucleus Interaction Experiment,” *Phys. Rev. D* **100** (2019) no. 9, 092005, [arXiv:1906.02200 \[physics.ins-det\]](#).
- [75] E. Depaoli *et al.*, “Deployment and performance of a Low-Energy-Threshold Skipper-CCD inside a nuclear reactor,” *JHEP* **10** (2024) 155, [arXiv:2401.07885 \[hep-ex\]](#).
- [76] P. Du, D. Egana-Ugrinovic, R. Essig, and M. Sholapurkar, “Sources of Low-Energy Events in Low-Threshold Dark-Matter and Neutrino Detectors,” *Phys. Rev. X* **12** (2022) no. 1, 011009, [arXiv:2011.13939 \[hep-ph\]](#).
- [77] P. Du, D. Egaña Ugrinovic, R. Essig, and M. Sholapurkar, “Low-energy radiative backgrounds in CCD-based dark-matter detectors,” *JHEP* **01** (2024) 164, [arXiv:2310.03068 \[hep-ph\]](#).
- [78] A. Berlin, N. Blinov, G. Krnjaic, P. Schuster, and N. Toro, “Dark Matter, Millicharges, Axion and Scalar Particles, Gauge Bosons, and Other New Physics with LDMX,” *Phys. Rev. D* **99** (2019) no. 7, 075001, [arXiv:1807.01730 \[hep-ph\]](#).
- [79] K. J. Kelly and Y.-D. Tsai, “Proton fixed-target scintillation experiment to search for millicharged dark matter,” *Phys. Rev. D* **100** (2019) no. 1, 015043, [arXiv:1812.03998 \[hep-ph\]](#).
- [80] C. Boehm, M. J. Dolan, and C. McCabe, “A Lower Bound on the Mass of Cold Thermal Dark Matter from Planck,” *JCAP* **08** (2013) 041, [arXiv:1303.6270 \[hep-ph\]](#).
- [81] C. Creque-Sarbinowski, L. Ji, E. D. Kovetz, and M. Kamionkowski, “Direct millicharged dark matter cannot explain the EDGES signal,” *Phys. Rev. D* **100** (2019) no. 2, 023528, [arXiv:1903.09154 \[astro-ph.CO\]](#).
- [82] L. J. Hall, K. Jedamzik, J. March-Russell, and S. M. West, “Freeze-In Production of Fimp Dark Matter,” *JHEP* **1003** (2010) 080, [arXiv:0911.1120 \[hep-ph\]](#).
- [83] X. Chu, T. Hambye, and M. H. G. Tytgat, “The Four Basic Ways of Creating Dark Matter Through a Portal,” *JCAP* **1205** (2012) 034, [arXiv:1112.0493 \[hep-ph\]](#).
- [84] C. Dvorkin, T. Lin, and K. Schutz, “Making Dark Matter Out of Light: Freeze-In from Plasma Effects,” *Phys. Rev. D* **99** (2019) no. 11, 115009, [arXiv:1902.08623 \[hep-ph\]](#).
- [85] T. Emken, R. Essig, C. Kouvaris, and M. Sholapurkar, “Direct Detection of Strongly Interacting Sub-GeV Dark Matter via Electron Recoils,” *JCAP* **09** (2019) 070, [arXiv:1905.06348 \[hep-ph\]](#).

- [86] K. K. Boddy, V. Gluscevic, V. Poulin, E. D. Kovetz, M. Kamionkowski, and R. Barkana, “Critical assessment of CMB limits on dark matter-baryon scattering: New treatment of the relative bulk velocity,” *Phys. Rev. D* **98** (2018) no. 12, 123506, [arXiv:1808.00001 \[astro-ph.CO\]](#).
- [87] R. Harnik, R. Plestid, M. Pospelov, and H. Ramani, “Millicharged cosmic rays and low recoil detectors,” *Phys. Rev. D* **103** (2021) no. 7, 075029, [arXiv:2010.11190 \[hep-ph\]](#).
- [88] D. Dunsky, L. J. Hall, and K. Harigaya, “CHAMP Cosmic Rays,” *JCAP* **07** (2019) 015, [arXiv:1812.11116 \[astro-ph.HE\]](#).
- [89] **XENON** Collaboration, E. Aprile *et al.*, “Low-mass dark matter search using ionization signals in XENON100,” *Phys. Rev. D* **94** (2016) no. 9, 092001, [arXiv:1605.06262 \[astro-ph.CO\]](#). [Erratum: *Phys.Rev.D* 95, 059901 (2017)].
- [90] M. Laletin and J.-R. Cudell, “Strongly interacting dark matter and the DAMA signal,” *JCAP* **07** (2019) 010, [arXiv:1903.04637 \[hep-ph\]](#).
- [91] J. Rich, R. Rocchia, and M. Spiro, “A Search for Strongly Interacting Dark Matter,” *Phys. Lett.* **B194** (1987) 173. [,221(1987)].
- [92] M. S. Mahdawi and G. R. Farrar, “Constraints on Dark Matter with a moderately large and velocity-dependent DM-nucleon cross-section,” *JCAP* **1810** (2018) no. 10, 007, [arXiv:1804.03073 \[hep-ph\]](#).
- [93] A. Prabhu and C. Blanco, “Constraints on dark matter-electron scattering from molecular cloud ionization,” *Phys. Rev. D* **108** (2023) no. 3, 035035, [arXiv:2211.05787 \[hep-ph\]](#).
- [94] J. B. Muñoz and A. Loeb, “A small amount of mini-charged dark matter could cool the baryons in the early Universe,” *Nature* **557** (2018) no. 7707, 684, [arXiv:1802.10094 \[astro-ph.CO\]](#).
- [95] H. Vogel and J. Redondo, “Dark Radiation constraints on minicharged particles in models with a hidden photon,” *JCAP* **02** (2014) 029, [arXiv:1311.2600 \[hep-ph\]](#).
- [96] **LDMX** Collaboration, T. Åkesson *et al.*, “Light Dark Matter eXperiment (LDMX),” [arXiv:1808.05219 \[hep-ex\]](#).
- [97] **NA64** Collaboration, Y. M. Andreev *et al.*, “Search for Light Dark Matter with NA64 at CERN,” *Phys. Rev. Lett.* **131** (2023) no. 16, 161801, [arXiv:2307.02404 \[hep-ex\]](#).
- [98] **DUNE** Collaboration, D. Jena, “The DUNE Experiment,” *PoS HQL2023* (2024) 023.
- [99] **SHiP, SHIP** Collaboration, C. Ahdida *et al.*, “The SHiP experiment at the proposed CERN SPS Beam Dump Facility,” *Eur. Phys. J. C* **82** (2022) no. 5, 486, [arXiv:2112.01487 \[physics.ins-det\]](#).
- [100] **FASER** Collaboration, A. Ariga *et al.*, “FASER: ForwArd Search ExpeRiment at the LHC,” [arXiv:1901.04468 \[hep-ex\]](#).
- [101] **SND@LHC, SHiP** Collaboration, E. Graverini, “A roadmap for neutrino detection at LHC, HL-LHC and SPS,” *Nucl. Instrum. Meth. A* **1068** (2024) 169804, [arXiv:2408.15851 \[hep-ex\]](#).
- [102] B. Batell, J. L. Feng, and S. Trojanowski, “Detecting Dark Matter with Far-Forward Emulsion and Liquid Argon Detectors at the LHC,” *Phys. Rev. D* **103** (2021) no. 7, 075023, [arXiv:2101.10338 \[hep-ph\]](#).
- [103] J. L. Feng *et al.*, “The Forward Physics Facility at the High-Luminosity LHC,” [arXiv:2203.05090 \[hep-ex\]](#).
- [104] Online. https://pdg.lbl.gov/2022/AtomicNuclearProperties/HTML/shielding_concrete.html.
- [105] Online. https://pdg.lbl.gov/2014/AtomicNuclearProperties/HTML/standard_rock.html.

- [106] D. Snowden-Ifft, I. Ehle, J. L. Gauvreau, G. Gregory, N. Ma, J. L. Harton, F. G. Schuckman, D. S. Warner, M. Battaglieri, A. Bersani, A. Celentano, R. D. Vita, E. Fanchini, L. Marsicano, P. Musico, F. Panza, M. Ripani, E. Santopinto, N. Randazzo, G., Russo, E. Pasyuk, and E. Smith, “Beam-dump dark matter search utilizing a low-threshold, directional dark matter detector (bdx-drift) at jefferson lab,” 2019. <https://api.semanticscholar.org/CorpusID:210924875>.
- [107] **SuperCDMS** Collaboration, M. F. Albakry *et al.*, “First Measurement of the Nuclear-Recoil Ionization Yield in Silicon at 100 eV,” *Phys. Rev. Lett.* **131** (2023) no. 9, 091801, [arXiv:2303.02196](https://arxiv.org/abs/2303.02196) [[physics.ins-det](#)].
- [108] R. Essig, M. Sholapurkar, and T.-T. Yu, “Solar Neutrinos as a Signal and Background in Direct-Detection Experiments Searching for Sub-GeV Dark Matter With Electron Recoils,” *Phys. Rev. D* **97** (2018) no. 9, 095029, [arXiv:1801.10159](https://arxiv.org/abs/1801.10159) [[hep-ph](#)].
- [109] Y. Sarkis, A. Aguilar-Arevalo, and J. C. D’Olivo, “Ionization efficiency for nuclear recoils in silicon from about 50 eV to 3 MeV,” *Phys. Rev. A* **107** (2023) no. 6, 062811, [arXiv:2209.04503](https://arxiv.org/abs/2209.04503) [[physics.atom-ph](#)].